

## Research Paper

# Characterizing the spectral, microstructural, and chemical effects of solar wind irradiation on the Murchison carbonaceous chondrite through coordinated analyses



D.L. Laczniak <sup>a,\*</sup>, M.S. Thompson <sup>a</sup>, R. Christoffersen <sup>b</sup>, C.A. Dukes <sup>c</sup>, S.J. Clemett <sup>b</sup>, R.V. Morris <sup>d</sup>, L.P. Keller <sup>d</sup>

<sup>a</sup> Department of Earth, Atmospheric, and Planetary Sciences, Purdue University, 550 Stadium Mall Drive, West Lafayette, IN 47907, United States of America

<sup>b</sup> Jacobs, NASA Johnson Space Center, Mail Code X13, Houston, TX 77058, United States of America

<sup>c</sup> Materials Science and Engineering, University of Virginia, 395 McCormick Road, Charlottesville, VA 22904, United States of America

<sup>d</sup> ARES, NASA Johnson Space Center, Mail Code X13, Houston, TX 77058, United States of America

## ARTICLE INFO

## ABSTRACT

**Keywords:**

Space weathering  
Solar wind  
Carbonaceous asteroid analog  
Asteroidal regolith  
Electron microscopy

We performed H<sup>+</sup> and He<sup>+</sup> irradiation experiments on slabs of the Murchison CM2 meteorite to simulate solar wind irradiation of carbonaceous asteroids. Two separate 6 mm × 6 mm regions were irradiated with 1 keV H<sup>+</sup> and 4 keV He<sup>+</sup>, respectively, to fluences of  $8.1 \times 10^{17}$  ions/cm<sup>2</sup> for H<sup>+</sup> and  $1 \times 10^{18}$  ions/cm<sup>2</sup> for He<sup>+</sup>. Unirradiated and irradiated surfaces were analyzed using X-ray photoelectron spectroscopy (XPS), visible to near-infrared spectroscopy (VNIR; 0.35–2.5 μm), and microprobe two-step laser-desorption mass spectrometry (μL<sup>2</sup>MS). We also performed analytical field-emission scanning transmission electron microscopy (FE-STEM) on focused ion beam (FIB) cross-sections extracted from olivine grains and matrix material within the H<sup>+</sup>- and He<sup>+</sup>-irradiated regions. In situ XPS analyses suggest that ion irradiation results in the removal of most surface carbon and the partial reduction of surface iron to lower oxidation states. In response to He<sup>+</sup>-irradiation, we observe brightening (longward of ~0.75 μm) and reddening of reflectance spectra, which is a departure from typical lunar-style space weathering. Additionally, H<sup>+</sup>- and He<sup>+</sup>-irradiation have opposing effects on organic carbon content: H<sup>+</sup>-irradiation increases the abundance of some low-molecular-weight free organic species by breaking down macromolecular material while He<sup>+</sup>-irradiation causes a decrease in overall organic content by cleaving bonds and sputtering constituent atoms. This suggests that solar wind H<sup>+</sup>-irradiation and solar wind He<sup>+</sup>-irradiation change the organic functional group chemistry of asteroidal regolith in different ways. In contrast to some previous experimental space weathering studies, we observe an increase in H<sub>2</sub>O and OH<sup>-</sup> abundances in our sample in response to both types of ion irradiation. FE-STEM and energy dispersive X-ray spectroscopy (EDX) analyses show complete amorphization of matrix phyllosilicates in ion-affected rims, partial amorphization of olivine, and changes in Si and Mg concentrations at and/or near the surface. We discuss the implications of these results for understanding the complex nature of space weathering on primitive, carbon-rich asteroids and for analyzing future returned samples from carbonaceous asteroids Bennu and Ryugu.

## 1. Introduction

Space weathering processes—driven predominantly by micrometeoroid impacts and solar wind irradiation—progressively alter the optical, microstructural, and chemical properties of regolith grains on airless planetary surfaces across the solar system (Hapke, 2001; Pieters and Noble, 2016). Micrometeoroid bombardment modifies regolith through comminution (the breaking apart of grains), impact melting, shock,

vaporization, recondensation, and impact gardening (excavation of buried grains). In contrast, solar wind ions (mostly H<sup>+</sup> and He<sup>+</sup>) are implanted into grain surfaces where they change microstructure and solid-state chemistry through vesiculation, amorphization, diffusion, sputtering, and sputter re-deposition. Both space weathering processes can produce submicroscopic Fe-bearing particles, which significantly alter the spectral characteristics of planetary surfaces and, in turn, complicate the interpretation of remote sensing spacecraft data and the

\* Corresponding author.

E-mail address: [dlacznia@purdue.edu](mailto:dlacznia@purdue.edu) (D.L. Laczniak).

pairing of meteorites to their parent asteroids (e.g., ordinary chondrites with S-type asteroids) (e.g., Britt et al., 1992; Clark et al., 2002; Gaffey et al., 1993; Morris, 1976; Pieters et al., 2000). By analyzing returned samples and conducting laboratory experiments, we can better understand the complex physical, chemical, and spectral effects of space weathering and the role of this process in the evolution of airless planetary surfaces.

Evidence of space weathering was first recognized in visible to mid-infrared spectra (VIS-IR;  $\sim 0.4\text{--}5.0\ \mu\text{m}$ ) of lunar samples returned by the Apollo missions. Compared to material from rock interiors, lunar regolith exhibited redder spectral slopes (increase in reflectance with increasing wavelength), weaker absorption bands, and lower albedo (decreased reflectance) (Adams and McCord, 1971a, 1971b, 1973). A combination of transmission electron microscope (TEM) studies of microstructurally and chemically distinct grain rims in lunar soils (e.g., Housley et al., 1973; Keller and McKay, 1993, 1997) and spectroscopic analyses of lunar soil size fractions (e.g., Allen et al., 1993; Pieters et al., 1993) ultimately identified submicroscopic metallic Fe particles (also known as nanophase Fe particles, or npFe<sup>0</sup>) as the primary cause of spectral discrepancies between fresh and space-weathered lunar samples. Specifically, the size and abundance of these particles were shown to control optical properties, with larger npFe<sup>0</sup> ( $>40\ \text{nm}$  in diameter) causing darkening and smaller npFe<sup>0</sup> ( $<40\ \text{nm}$  in diameter) causing both reddening and darkening (Keller et al., 1998; Lucey and Noble, 2008; Lucey and Riner, 2011; Noble et al., 2007). Aside from npFe<sup>0</sup>, amorphization, vesiculation, near-surface cation depletion, and accumulation of elements not indigenous to the host mineral were also observed in lunar soil grain rims (Keller and McKay, 1997).

More recently, thousands of regolith particles from the surface of near-Earth, S-type asteroid Itokawa were returned by the Japan Aerospace Exploration Agency's (JAXA) Hayabusa mission (Nakamura et al., 2011). While the compositions of these particles are similar to LL5–6 ordinary chondrites (Nakamura et al., 2011), the spectral reflectance of Itokawa's surface is both redder and darker than the spectral reflectance of its meteoritic counterpart, suggesting that space weathering processes have altered the surface of this S-type asteroid (Abe et al., 2006; Hiroi et al., 2006). TEM analyses of Itokawa regolith particles have revealed many lunar-like space weathering features such as melt and vapor deposits, vesiculated textures, and partially to completely amorphous grain rims (Keller and Berger, 2014; Noguchi et al., 2011, 2014a, 2014b; Thompson et al., 2014). However, unlike lunar samples, Itokawa grains contain chemically diverse, opaque, nanometer-scale particles, including nanophase-Fe-S (npFeS), np(Fe,Mg)S, and npFe<sup>0</sup> (Noguchi et al., 2011, 2014a, 2014b).

Laboratory experiments also provide important insight into space weathering processes on airless bodies. Pulsed-laser irradiation is commonly used to simulate micrometeoroid bombardment (e.g., Loefler et al., 2009; Sasaki et al., 2001; Yamada et al., 1999), because it replicates the high temperature, short-duration thermal events associated with high-velocity dust particle ( $1\text{--}10\ \mu\text{m}$  in size) impacts. Similarly, 1 keV H<sup>+</sup> and 4 keV He<sup>+</sup> ion bombardment is used to simulate solar wind irradiation (Bradley et al., 1996; Carrez et al., 2002; Dukes et al., 1999; Hapke, 1973; Keller et al., 2015a; Loeffler et al., 2009), which consists mostly of low energy (1 keV/amu) H<sup>+</sup> and He<sup>+</sup> ions ( $\sim 96\%\ \text{H}^+$ ,  $\sim 4\%\ \text{He}^+$ ) (Gosling, 2007; Johnson, 1990). Synthesizing results from returned sample analyses and laboratory experiments has significantly improved our understanding of space weathering for the Moon and S-type asteroids. However, our understanding of space weathering on carbonaceous (C-complex) asteroids, which dominate the outer main belt and contain both hydrated silicate and organic phases (e.g., Bland et al., 2004; Cloutis et al., 2011b; DeMeo et al., 2015), is at an early stage. This situation will change with the return of carbonaceous samples to Earth from asteroids Bennu (NASA OSIRIS-REx) (Lauretta et al., 2017) and Ryugu (JAXA Hayabusa2) (Watanabe et al., 2017). Prior to sample return, laboratory simulations using carbonaceous analog materials are necessary for understanding how space weathering

changes the optical, microstructural, and chemical properties of carbonaceous regolith, for accurately interpreting remote sensing spacecraft data, and for analyzing future returned samples from Bennu and Ryugu.

Pulsed-laser irradiation studies of carbonaceous chondrites and relevant minerals have demonstrated a range of spectral effects such as overall darkening with reddening in some samples and bluing in others, wavelength-dependent bluing or reddening, transitions from bluing to reddening (or reddening to bluing) with continued laser irradiation, and initial darkening followed by brightening with continued laser exposure (Gillis-Davis et al., 2013, 2015, 2017; Hiroi et al., 2013; Kaluna et al., 2017; Matsuoka et al., 2015; Prince et al., 2020; Thompson et al., 2019, 2020). Coordinated analyses of laser-irradiated carbonaceous chondrites have attributed these complex and variable spectral results to microstructural and chemical products including melt/vapor deposits, phyllosilicate amorphization, vesiculation, and the formation of metallic Fe, Fe-sulfide, Fe-Ni-sulfide, and Fe-oxide nanoparticles (Gillis-Davis et al., 2017; Thompson et al., 2019, 2020). Most recently, incremental heating of Murchison resulted in the decomposition of matrix tochilinite and serpentine and the formation of submicrometer- to micrometer-sized Fe-rich olivine ( $\sim\text{Fo}_{56}$ ), magnetite, sulfides, and Fe-Ni metals. TEM analysis showed that Murchison heated to 800 °C contains many Fe-Ni-S nanoparticles in its fine-grained matrix (Lee et al., 2020; Morris et al., 2020).

Similarly, ion irradiation experiments simulating solar wind bombardment of carbonaceous chondrites also observed conflicting spectral trends, including darkening and reddening, brightening and bluing, and minimal changes (Brunetto et al., 2014; Brunetto and Strazzulla, 2005; Lantz et al., 2015, 2017; Vernazza et al., 2013). All these studies also observed attenuation of characteristic absorption bands. While many investigations detected a longward shift in the position of the  $3\ \mu\text{m}\ \text{OH}^-/\text{H}_2\text{O}$  and  $10\ \mu\text{m}$  silicate bands—the latter being associated with preferential sputtering of Mg and amorphization of Mg-rich phases—low energy (4 keV He<sup>+</sup>) irradiation experiments performed by Keller et al. (2015b) did not produce this longward shift. Recently, Nakamura et al. (2020) confirmed the ion energy dependence of optical signatures by comparing reflectance spectra of Murchison samples irradiated with 20 keV He<sup>+</sup> versus 4 keV He<sup>+</sup>. Initially, 20 keV He<sup>+</sup> irradiation induced slight darkening and reddening at visible and infrared wavelengths, but with continued exposure, brightening and bluing occurred. In contrast, 4 keV He<sup>+</sup> irradiation continually caused darkening and reddening, leading to more significant spectral changes overall.

Coordinated analyses investigating microstructural and chemical changes in ion irradiated carbonaceous chondrites, in addition to spectral signatures, are limited. Scanning and transmission electron microscopy analyses of a Murchison sample irradiated with 4 keV He<sup>+</sup> showed surface blistering, vesiculated textures, phyllosilicate amorphization, and the formation of S- and Ni-bearing Fe nanoparticles in matrix material (Keller et al., 2015a, 2015b, 2015c). Subsequent electron energy loss spectroscopy (EELS) measurements indicated a reduction of Fe<sup>3+</sup> to Fe<sup>2+</sup> and loss of O bound as OH<sup>-</sup> (Keller et al., 2015b, 2015c). In addition to inorganic components, experiments have been conducted to investigate the effect of solar wind irradiation on organic phases, using natural bitumens (i.e., asphaltites, kerites, and anthraxolites) as analogs for extraterrestrial refractory organics (Court et al., 2006; Court and Sephton, 2012; Moroz et al., 2004). Results show that ion irradiation causes brightening and bluing of VNIR spectra from carbonization (i.e., hydrogen loss), polymerization of low-molecular-weight compounds, and an increase in the concentration of polycyclic aromatic hydrocarbons (PAHs), among other effects (Court et al., 2006; Court and Sephton, 2012; Moroz et al., 2004). Similar studies using carbonaceous chondrites have shown that He<sup>+</sup> and Ar<sup>+</sup> irradiation lead to amorphization and disordering of organic carbon (Brunetto et al., 2014; Lantz et al., 2015). Recently, Thompson et al. (2020) observed an increase in the abundance of PAH species like naphthalene, phenanthrene, and pyrene in pulsed-laser irradiated Murchison samples, which was attributed to the

depolymerization of macromolecular insoluble organic matter (IOM).

To build on these results, we simulate solar wind exposure on carbonaceous asteroids by irradiating the Murchison meteorite with  $H^+$  and  $He^+$  ions. We discuss the optical, microstructural, and chemical effects of ion bombardment in the organic and inorganic components of Murchison. By correlating detailed microstructural and chemical analyses with spectroscopic observations, results from this study contribute to a more comprehensive understanding of space weathering of carbonaceous regolith and provide an experimental comparison for future laboratory analyses of OSIRIS-REx and Hayabusa2 returned samples.

## 2. Materials and methods

We performed our experiments on saw-cut, flat pieces of the Murchison (CM2) meteorite. Murchison is considered to be a suitable meteoritic analog for material on the surface of B-type asteroid Bennu because of its spectral similarity to this asteroid over the 0.4–2.4  $\mu m$  wavelength region (Clark et al., 2011; Lauretta et al., 2019). Using a wafer saw, we dry cut a ~12 mm × 8 mm × 1 mm slab from the allocated Murchison material and roughened the surface with 400 grit silicon carbide grinding paper to more closely approximate natural grains on asteroid surfaces and reduce specular reflection during spectral analysis. Scanning electron microscope and transmission electron microscope imaging did not reveal any contamination layers or particulates on the Murchison surface at the micro- or nanoscale resulting from this grinding procedure.

### 2.1. Experimental procedure

In order to investigate the individual roles of each principal solar wind ion,  $H^+$  and  $He^+$  irradiations were performed separately on two

discrete 6 mm × 6 mm regions of the same Murchison slab at the University of Virginia's (UVA) Laboratory for Astrophysics and Surface Physics (Fig. 1A). The sample was mounted in an ultra-high vacuum (UHV) chamber ( $10^{-8}$  Pa) such that the ion beam was oriented normal to the surface of the slab. A Faraday cup was used to measure ion fluxes before and after each experiment. An electron neutralizer was operated simultaneous with irradiation, continuously inundating the sample surface with low energy (<1 eV) electrons to prevent electrostatic charging. Using a flux of  $1.9 \times 10^{13}$  ions/ $cm^2$ ·s, the first region was irradiated with 1 keV  $H^+$  to a total fluence of  $8.1 \times 10^{17}$  ions/ $cm^2$  (~700 yrs. of exposure at Bennu). Using a flux of  $1.0 \times 10^{13}$  ions/ $cm^2$ ·s, the second region was irradiated with 4 keV  $He^+$  to a total fluence of  $1.1 \times 10^{18}$  ions/ $cm^2$  (~23,000 yrs. of exposure at Bennu). Considering collision cooling occurs at  $\sim 10^{-12}$  s timescales, the fluxes used here are sufficiently low such that they can be described by standard linear cascade theory with no correction required for thermal effects which occur with overlapping damage cascades (Sigmund, 1981).

To determine the solar wind exposure times that our experiments simulate, we approximated the  $H^+$  and  $He^+$  fluxes at 1.126 AU—the semimajor axis of Bennu's orbit (Lauretta et al., 2015). Using relative ion abundances of ~96%  $H^+$  and ~4%  $He^+$  and the inverse relationship between solar wind flux and heliocentric distance ( $R^{-2}$ ) (Gosling, 2007), we estimated incident ion fluxes of  $\sim 1.5 \times 10^8 H^+/cm^2$ ·s and  $\sim 6.1 \times 10^6 He^+/cm^2$ ·s at asteroid Bennu. Following the mathematical procedure given by Loeffler et al. (2009), we divided these fluxes by a factor of four to determine the average ion flux striking a rotating sphere. Based on these fluxes, our experimental  $H^+$  and  $He^+$  fluences correspond to total solar wind direct exposure times at Bennu of approximately 700 years and 23,000 years, respectively.

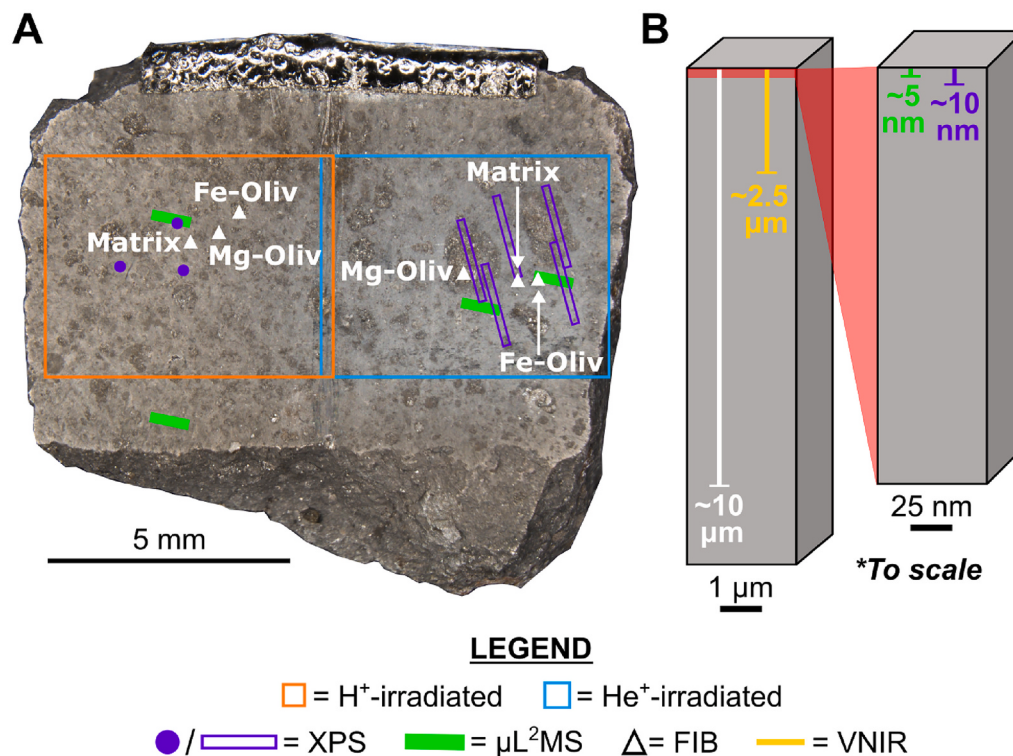


**Fig. 1.** (A) Stereoscope image of the Murchison slab surface showing locations of the  $H^+$ -irradiated (orange outline) and  $He^+$ -irradiated (blue outline) regions as well as the XPS (purple points and rectangles),  $\mu L^2 MS$  (green rectangles), and FIB locations (white triangles). The VNIR beam (~7 mm) was centered in the middle of the slab to acquire the unirradiated spectrum. For the  $H^+$ - and  $He^+$ -irradiated spectra, the VNIR beam was placed in the middle of each irradiated region (not indicated in panel A). Note that XPS spectra were acquired from the  $H^+$ -irradiated region in spot mode using a 100  $\mu m$  beam while  $He^+$ -irradiated XPS spectra were acquired in line scan mode (100  $\mu m$  beam was rastered over a 1.4 mm long region). All other analytical parameters remained identical for all XPS acquisitions. (B) Diagram (cross sectional-view, to scale) comparing the information depths of XPS (purple), VNIR (yellow), and  $\mu L^2 MS$  (green) analyses. The approximate depth of extracted FIB-sections (white) is also indicated. Note that spectroscopy probes depths on the order of the wavelength of the incident illumination. In (B), we indicate the maximum VNIR information depth which is constrained by the upper limit of the wavelength range used in this study (i.e., 2.5  $\mu m$ ). (For interpretation of the references to colour

in this figure legend, the reader is referred to the web version of this article.)

## 2.2. X-ray photoelectron spectroscopy (XPS)

We investigated in situ changes in surface chemistry resulting from ion irradiation using UVA's PHI Versaprobe III Imaging X-ray Photoelectron Spectrometer (XPS) equipped with a monochromatic, scanning X-ray source ( $\text{AlK}_{\alpha 1}$ : 1486.6 eV) and hemispherical electron-energy analyzer under ultra-high vacuum (base pressure:  $10^{-8}$ – $10^{-9}$  Pa). XPS analysis provides quantitative elemental abundance and chemical information (e.g., oxidation states) for the outermost ~10 nm of sample surfaces (Fig. 1B) with a sensitivity <0.1 atom.%. Survey (wide scan) spectra were acquired both before and after each type of ion irradiation. High-resolution (narrow scan) spectra of the elements O, C, S, Al, Si, Mg, and Fe were acquired from the  $\text{H}^+$ -irradiated region. A pass energy of 224 eV was used for survey spectra and 26 eV for high-resolution spectra, resulting in energy resolutions of 2.20 eV and 0.25 eV, respectively. All XPS analyses employed a 100  $\mu\text{m}$ -diameter beam, however,  $\text{H}^+$ -irradiated spectra were acquired in spot mode while  $\text{He}^+$ -irradiated spectra were acquired in line scan mode (i.e., the 100  $\mu\text{m}$  beam was rastered over a 1.4 mm long region) to mitigate radiation damage. Analyzer parameters were identical for both experiments. In total, we collected spectra from three matrix-bearing regions in the  $\text{H}^+$  experiment. For the  $\text{He}^+$  experiment, we collected spectra from five regions: one from the matrix, two from chondrules, and two from a region containing both matrix and chondrules (the latter group consists mostly of matrix material) (Fig. 1A). Dual-beam charge neutralization was used to compensate for photoelectron emission during XPS analysis.

Data processing was performed using ULVAC-PHI's MultiPak 9.8.0.19 software. Following procedures employed by Dukes et al. (1999), Loeffler et al. (2009), and Powell et al. (1979), we corrected spectra for any relative shifts in binding energy caused by changes in the spectrometer work function, electrostatic charging, or over/under neutralization during analysis by aligning Si2p oxide peaks for each spectrum to the same binding energy. Next, we calibrated the absolute binding energy scale to the adventitious (i.e., contaminant sourced from ambient environment) carbon peak (284.8 eV) in the unirradiated spectra, which is present at the sample's surface because of atmospheric contamination. For chemical analysis using high-resolution spectra, photoelectron peaks were fit with Gaussian-Lorentzian (or asymmetric Gaussian-Lorentzian where appropriate) functions after subtraction of a Shirley background.

## 2.3. Reflectance spectroscopy

Visible to near-infrared (VNIR; 0.35–2.5  $\mu\text{m}$ ) optical spectra were obtained under ambient laboratory conditions from pre- and post-irradiated surfaces using the fiber-optic ASD FieldSpec 3 Hi-Res Spectroradiometer at NASA Johnson Space Center (JSC). This instrument has a beam diameter of ~7 mm and spectral resolutions of 3 nm at 700 nm, 8.5 nm at 1400 nm, and 6.5 nm at 2100 nm. The probe has an incandescent light source mounted in a parabolic reflector whose axis is held at an angle of 35° from the surface normal (incident angle). The fiber axis is positioned at an angle of 12° from the surface normal (emission angle) and the phase angle is 23°. To account for spectral effects, specifically with respect to band centers and intensities, resulting from slab misalignment (i.e., non-parallel alignment with the surface normal to the Muglight axis) or orientation, we acquired at least 10 spectra from the unirradiated,  $\text{H}^+$ -irradiated, and  $\text{He}^+$ -irradiated surfaces, rotating the Murchison slab 90° between each measurement. No spectral dependence on slab orientation was noted. The final VNIR spectrum for these surfaces is the average of measurements acquired at varied azimuth angles. While it is possible that the instrument beam partially overlapped into the unirradiated region when acquiring spectra from the  $\text{H}^+$ - and  $\text{He}^+$ -irradiated regions, this overlap was small and its contribution to the final spectrum is minor. Spectra were calibrated against a Labsphere Spectralon white (99%) reference panel and converted to absolute reflectance. We used the Environment for Visualizing Images

(ENVI) software from Harris Geospatial Solutions to calculate continuum-removed spectra from absolute reflectance.

## 2.4. Microprobe two-step laser-desorption mass spectrometry ( $\mu\text{L}^2\text{MS}$ )

We used a microprobe two-step laser-desorption mass spectrometer ( $\mu\text{L}^2\text{MS}$ ) at NASA JSC to investigate changes in organic functional group chemistry resulting from  $\text{H}^+$ - and  $\text{He}^+$ -irradiation (Clemett and Zare, 1997; Clemett et al., 2014; Hanley and Zimmermann, 2009; Shi and Lipson, 2005). Organic molecules are first desorbed as neutral species from the sample surface (uppermost ~5 nm, Fig. 1B) using a focused pulsed  $\text{CO}_2$  infrared (IR) laser (150 ns pulse at 10.6  $\mu\text{m}$  wavelength; 5–7  $\mu\text{m}$  spot diameter). After a suitable time delay (45  $\mu\text{s}$ ), the desorbed species are photoionized using either an ultraviolet (UV) or vacuum ultraviolet (VUV) laser pulse (4th & 9th harmonics of Nd:YAG laser). The types of organic molecules that are ionized depends on the wavelength of the photoionization source. Here, we employed VUV laser photoionization (118 nm) which is capable of ionizing virtually all aliphatic and aromatic organic species (Clemett and Zare, 1997; Clemett et al., 2014; Hanley and Zimmermann, 2009; Shi and Lipson, 2005).

The masses of the ionized organic molecules are measured using a reflectron time-of-flight (TOF) spectrometer. Conversion of TOF spectra to mass spectra was made using a calibrated gas-phase mass reference mixture of acetone ( $\text{CH}_3\text{COCH}_3$ ), hexane ( $\text{C}_6\text{H}_6$ ) and toluene ( $\text{C}_6\text{H}_5\text{CH}_3$ ) that can be introduced into the vacuum chamber using a calibrated leak (Clemett and Zare, 1997; Clemett et al., 2014). Following the ion irradiation experiments, we acquired summed mass spectra from one unirradiated, one  $\text{H}^+$ -irradiated, and two  $\text{He}^+$ -irradiated regions of the Murchison sample to identify organic functional group chemistry (Fig. 1A). To compare organic compositions effectively, we removed the large  $^{32}\text{S}_2$  peak ( $m/z \sim 63.944$ ) associated with metal sulfides from the spectra (sulfur species have particularly high VUV ionization cross-sections). We also collected spatial maps ( $500 \times 2000 \mu\text{m}^2$ ) at the 118 nm wavelength of the same unirradiated,  $\text{H}^+$ -irradiated, and  $\text{He}^+$ -irradiated regions from which summed spectra were extracted. These maps represent the sum of organic species with masses between 20 and 250  $m/z$  and show their spatial distribution and abundance at a spatial resolution of ~5  $\mu\text{m}$ .

## 2.5. Field-emission scanning transmission electron microscopy (FE-STEM)

The Murchison slab was mounted onto an aluminum scanning electron microscope (SEM) stub (12.7 mm diameter) with a thin film of epoxy. We used the FEI Quanta 3D focused ion beam scanning electron microscope (FIB-SEM) at JSC to prepare FIB cross-sections for transmission electron microscopy (TEM) analysis. FIB cross-sections were extracted from matrix material, Mg-rich olivine (~Fo<sub>99</sub>), and more Fe-rich olivine (~Fo<sub>55</sub>) in both the  $\text{H}^+$ - and  $\text{He}^+$ -irradiated Murchison regions, yielding six FIB-sections in total (Fig. 1A). Extending ~10  $\mu\text{m}$  in depth from the sample surface (Fig. 1B), each cross-section includes unaltered Murchison material that can be compared to the ion-irradiated near-surface of the sample to constrain microstructural and chemical changes derived from the irradiation process. It should be noted that chondrules in Murchison are largely ~Fo<sub>99</sub> in composition (Bland et al., 2004; Howard et al., 2009, 2011; Zolensky and McSween Jr., 1988). Thus, for the purpose of this paper, we henceforth refer to olivine samples with a composition < Fo<sub>99</sub> simply as “Fe-rich olivine.”

TEM analysis was performed using a JEOL 2500SE 200 kV field-emission scanning TEM (FE-STEM) at JSC. Conventional TEM, high-resolution TEM (HRTEM), bright field (BF) STEM, and high-angle annular dark field (HAADF) STEM images were acquired from each cross-section. Compositions of matrix cross-sections were characterized using a Thermo 50  $\text{mm}^2$  Si(Li) energy dispersive X-ray spectrometer (EDX) while compositions of olivine cross-sections were characterized using a recently installed JEOL SD60GV 60  $\text{mm}^2$  ultra-thin window

silicon drift detector (SDD). Both EDX detectors were supported by a Thermo System 7 pulse-processor EDX data analyzer. A combination of spot analyses, element maps, and line profiles were collected from each sample to understand element distributions, abundances, and ratios. Standard-based Cliff-Lorimer quantification was performed on all elemental maps and spot analyses in the Thermo NSS software using empirically determined K-factors. Most EDX element maps were obtained using a 2 nm probe to reduce beam damage. In a few instances, a 1 nm probe was used to increase spatial resolution. Element map pixel sizes were selected based on image magnification to prevent over- or under-sampling during raster scans.

## 2.6. SRIM simulations

We also modeled H<sup>+</sup> and He<sup>+</sup> ion damage and implantation as a function of depth for each of the primary phases of interest analyzed in this study (i.e., matrix phyllosilicates, Mg-rich olivine, and Fe-rich olivine) using the Stopping and Range of Ions in Matter (SRIM) Monte Carlo atomic collision code (Ziegler et al., 2010). Atomic displacement (i.e., damage) and implantation range profiles can be compared to thicknesses of ion-affected surface layers in our irradiated Murchison sample. These calculations used a value of 25 eV for the atomic displacement energy and an ion incidence angle normal to the target surface. For matrix phyllosilicate models, we used the density of serpentine (2.50 g/cm<sup>3</sup>)—the dominant phase in Murchison's matrix (e.g., Zolensky and McSween Jr., 1988; Burns and Fisher, 1994)—as the target density variable. For the Mg-rich (~Fo<sub>99</sub>) and Fe-rich (~Fo<sub>55</sub>) olivine models, we used target densities of 3.22 g/cm<sup>3</sup> and 4.00 g/cm<sup>3</sup>, respectively, however olivine composition has only a secondary effect on SRIM calculations. The single-ion differential curves for atomic vacancy production and implanted ion concentration were integrated and the vacancy concentrations converted to units of displacements per target atom (DPA) and implanted ion concentrations converted to atomic fractions. The single ion curves were then multiplied by the experimental fluences to produce the final DPA or implanted concentration curves for comparison to the experimental samples.

## 3. Results

### 3.1. X-ray photoelectron spectroscopy (XPS)

Survey XPS spectra from both matrix material and chondrules in the unirradiated, H<sup>+</sup>-irradiated, and He<sup>+</sup>-irradiated regions show that all measured surface chemistries (uppermost ~10 nm of the sample) contain C, O, Na, Mg, Al, Si, Ar, Ca, Fe, and Ni, with C content exhibiting the most significant change from ion irradiation (Fig. 2). The similarity in overall surface chemistry between matrix material and chondrules (i.e., the same elements are present in both phases) may result from beam overlap into non-targeted phases (i.e., the beam spot samples both chondrules and matrix material). Minor amounts of N are present in some unirradiated matrix surfaces which may reflect N-heterocycles, nucleobases, amino acids, or N heteroatoms of IOM in the Murchison meteorite (Cronin et al., 1985; Glavin et al., 2018, 2020; Pizzarello et al., 2006 and references therein; Schmitt-Kopplin et al., 2010). A small amount of F-contamination—likely from Teflon-sleeving near the X-ray source—appears on most surfaces and its abundance remains relatively unchanged after both H<sup>+</sup>- and He<sup>+</sup>-irradiation. Ar, which occurs in all unirradiated and irradiated matrix and chondrule surfaces ( $\leq 1$  atom.%), must be intrinsic to the sample. Considering the sensitivity limit of Ar is ~0.01%, this identification of Ar in our spectra suggests that the element is present in an amount greater than 1/10,000 atoms in the near surface region (~8 nm for 95% signal).

Survey XPS spectra show that He<sup>+</sup>-irradiation causes a large decrease in matrix and chondrule surface carbon content (~90%), reflecting the preferential sputtering of both intrinsic and adventitious carbon by He<sup>+</sup> irradiation (Fig. 2A and B). Atomic percent abundances reveal a slight

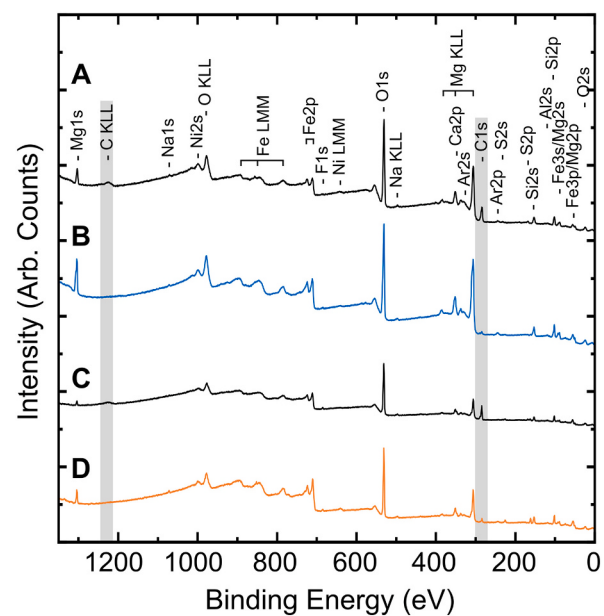


**Fig. 2.** Survey XPS spectra acquired from Murchison matrix material (A) before (black) and (B) after He<sup>+</sup>-irradiation (blue) and (C) before (black) and (D) after H<sup>+</sup>-irradiation (orange). Labels indicate elemental photoelectron (e.g., O1s) and Auger transition (e.g., O KLL) peaks. Ion irradiation causes significant attenuation of the C KLL and C1s peaks (locations indicated by grey boxes) likely associated with the removal of adventitious and intrinsic carbon. Argon is an intrinsic impurity in Murchison matrix phases while fluorine is a surface contaminant originating from either the instrument vacuum chamber or sample holder. All other elements appear as expected. (For interpretation of the references to colour in this figure legend, the reader is referred to the web version of this article.)

decrease in S content in both matrix and chondrule regions. Although less significant, Na content decreases by <35% in the matrix and <20% in chondrules. All other elements increase in concentration with the removal of surface species (e.g., carbon, sulfur) by He<sup>+</sup>-irradiation.

Similar to the He<sup>+</sup>-irradiated region, the most prominent change in surface chemistry from H<sup>+</sup>-irradiation is a reduction in carbon content (Fig. 2C and D), primarily intrinsic but some of which may be adventitious. Atomic percent surface abundances suggest an average decrease in carbon by 71% within the matrix. The average sulfur content also decreases by 12%. In matrix regions, all other elements—except F and Ni which stay relatively consistent in their abundance—increase in concentration after H<sup>+</sup>-irradiation, commensurate with the removal of carbon and analogous to observations of the He<sup>+</sup>-irradiated region.

High-resolution XPS datasets were collected from the H<sup>+</sup>-irradiation experiment to look for detectable changes in peak binding energies that might inform on changes in surface element oxidation state and/or peak ratios that might indicate small but detectable changes in surface chemistry (Fig. 3). Spectra for the C1s photoelectron region further support the decrease in carbon content observed in survey spectra (Fig. 3A). After deconvolution, high-resolution data exhibit three constituent carbon peaks at ~284.8 eV (C-C/C-H), ~286.2 eV (C-O-C), and ~288.6 eV (O-C=O), all of which attenuate in varying degrees with H<sup>+</sup>-irradiation. The C-C/C-H peak is the dominant feature (~91% carbon) and indicates the presence of polycyclic aromatic hydrocarbons (PAHs) and residual IOM (Barr and Seal, 1995; Vander Wal et al., 2011). This feature shifts slightly toward a lower binding energy after ion irradiation, indicating a transition in the carbon sp-hybridization toward a larger sp<sup>2</sup>:sp<sup>3</sup> ratio, which could imply the formation of aromatic graphite/graphene clusters such as those previously observed in irradiated asphaltite and kerite powders (Moroz et al., 2004).

As shown in Fig. 3B, H<sup>+</sup> bombardment also causes a reduction in the iron valence state. The Fe2p photoelectron features are comprised of a

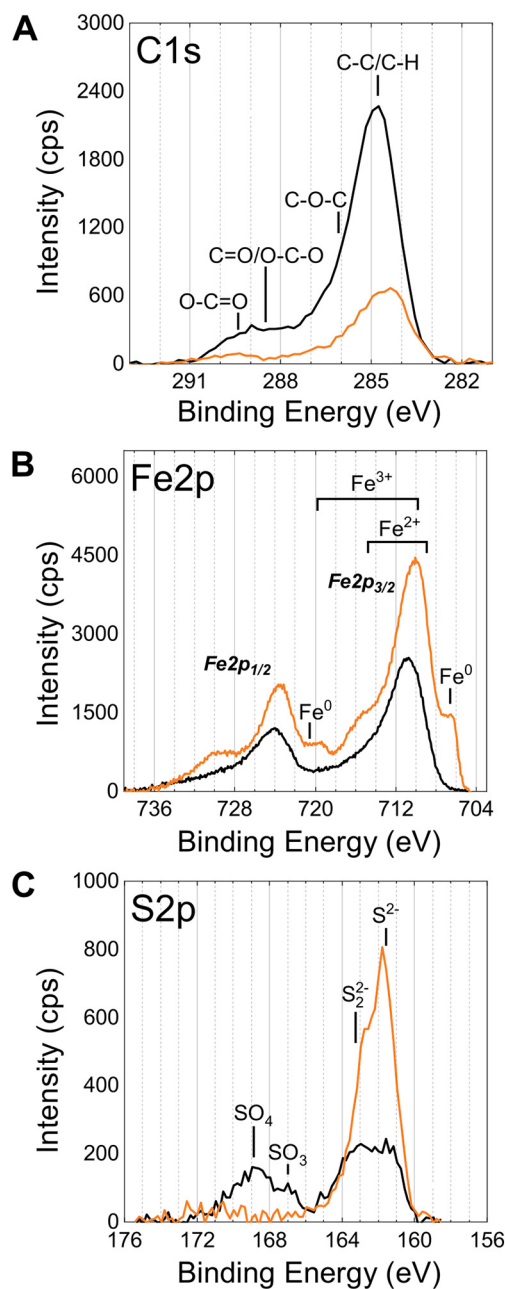


**Fig. 3.** High-resolution XPS spectra of the (A) C1s, (B) Fe2p, and (C) S2p regions before (black) and after (orange) H<sup>+</sup>-irradiation of the Murchison sample showing changes in elemental surface chemistry. H<sup>+</sup>-irradiation causes a decrease in surface carbon content (including both adventitious and intrinsic carbon), the chemical reduction of minor amounts of Fe, and the destruction/removal of surface sulfates.

spin quartet (Fe2p<sub>3/2</sub> and Fe2p<sub>1/2</sub>). Both oxide peaks also exhibit multiplet-splitting with unpaired electrons in the atom final state, as well as energy-loss features, which complicate interpretation. Spectra were deconvoluted into Fe2p<sub>3/2</sub> and Fe2p<sub>1/2</sub> peaks utilizing spectral fitting parameters provided by Biesinger et al. (2011). For the unirradiated matrix material, 91.6% of the iron was identified as Fe<sup>3+</sup> found in oxides and phyllosilicates [Fe2p<sub>3/2</sub> multiplet structure: 709.9 eV (27%), 710.9 eV (25%), 711.7 eV (19%), 712.8 eV (10%), 713.8 eV (10%), and 719.4 eV (9%)], 8.1% was Fe<sup>2+</sup> associated with olivine and phyllosilicates [Fe2p<sub>3/2</sub> multiplet structure: 708.5 eV (24%), 709.8 eV (30%), 711.0 eV (14.5%), 712.2 eV (25.5%), and 715.5 eV (6%)], and 0.2% appears as FeS [Fe2p<sub>3/2</sub> peak: ~706.5 eV (100%)]. After H<sup>+</sup>-irradiation,

a small amount of Fe<sup>3+</sup> and Fe<sup>2+</sup> is reduced to metallic iron, as evidenced by the growth of the peak at ~706.5 eV (Fe2p<sub>3/2</sub>) and ~720 eV (Fe2p<sub>1/2</sub>), resulting in a mixed iron metal/oxide/sulfide composition of: 74.6% Fe<sup>3+</sup>, 19.8% Fe<sup>2+</sup>, and 5.6% Fe<sup>0</sup>/FeS. Fe-Fe and Fe-S features appear at a similar binding energy for Fe2p, making it difficult to differentiate the native troilite from ion-induced Fe<sup>0</sup> (Biesinger et al., 2011; Terranova et al., 2018; Thomas et al., 2003).

Surface sulfates are identified, along with metal sulfide, disulfides and sulfite, in the unirradiated matrix regions of Murchison (Cant et al., 2015; Nesbitt et al., 1998; Thomas et al., 2003). These sulfates and sulfites are most likely exogenous to the Murchison sample, resulting from terrestrial alteration (Bland et al., 2006 and references therein). With H<sup>+</sup>-irradiation, the sulfates ( $\text{SO}_4^{2-}$ ) and sulfites ( $\text{SO}_3^{2-}$ ) are removed or reduced (Fig. 3C). Unirradiated S2p photoelectron spectra exhibit a sulfate peak at ~168.9 eV, sulfite at ~167.0 eV, disulfide ( $\text{S}_2^{2-}$ ) at 163.3 eV, and metal sulfide ( $\text{S}^{2-}$ ) at ~161.3 eV. Peak area analysis suggests that ~60% of surface sulfur occurs as sulfate. After H<sup>+</sup>-irradiation, only the sulfide (~82% sulfur) and disulfide peaks (~18% sulfur) remain, suggesting that matrix sulfate minerals are destroyed or removed by the preferential sputtering of oxygen atoms.

No noticeable change is observed in the binding energy of Mg, Al, or Si. The O1s photoelectron feature is the spectral envelope for all metal oxides (e.g., Fe-O; Mg-O, O-Si-O), sulfur-bearing molecules, water, and hydrocarbons present on the surface of the meteorite. While the development of a low-binding energy shoulder in the O1s region with H<sup>+</sup>-irradiation is consistent with the chemical reduction of metal and sulfur oxides, the O1s feature was not analyzed in detail in this study due to the large number and complexity of overlapping peaks.

### 3.2. Reflectance spectroscopy

Absolute reflectance spectra from the unirradiated, H<sup>+</sup>-irradiated, and He<sup>+</sup>-irradiated Murchison surfaces (Fig. 4A) all exhibit very low reflectance (<6.5%), consistent with Murchison spectra obtained by Cloutis et al. (2011b) and Lantz et al. (2015). The overall shape of these spectra closely resembles the Murchison chip spectrum from Cloutis et al. (2011b). It should be noted that Cloutis et al. (2011b) and Lantz et al. (2015) measured reflectance with different viewing geometries—illumination angles of 30° or 45°, respectively, and a constant collection angle of 0°—compared to our study. Albedos at different wavelengths in our unirradiated, H<sup>+</sup>-irradiated, and He<sup>+</sup>-irradiated spectra are shown in Table 1. The highest albedo occurs at ~0.55 μm for the unirradiated and H<sup>+</sup>-irradiated surfaces and at ~0.59 μm for the He<sup>+</sup>-irradiated surface. The H<sup>+</sup>-irradiated spectrum is very similar to the unirradiated surface in both brightness and slope (defined over the wavelength range from 0.65–2.5 μm), though minor reddening is observed longward of 0.65 μm. In contrast, the He<sup>+</sup>-irradiated spectrum is brighter above ~0.75 μm and ~57% redder than the unirradiated surface. Although they are not pronounced in the absolute reflectance spectra, some absorption bands are present, including a broad band centered at ~1.1 μm (phyllosilicates, olivine, and possibly magnetite) and small bands at ~1.95 μm (H<sub>2</sub>O) and ~2.2–2.35 μm (metal-OH).

Several absorption bands are observed in the continuum-removed reflectance of the unirradiated, H<sup>+</sup>-irradiated, and He<sup>+</sup>-irradiated surfaces (Fig. 4B). Many of these bands are characteristic of the Fe-bearing minerals that dominate Murchison's mineralogy such as tochilinite (hydrated Fe-Ni-S-O phase), cronstedtite (Fe<sup>2+</sup>-Fe<sup>3+</sup> phyllosilicate), and other Fe-Mg serpentine minerals (Bland et al., 2004; Cloutis et al., 2011b; Zolensky et al., 1993). The broad absorption between ~0.60 and 1.6 μm is formed by three minima characteristic of serpentine group minerals, including an absorption at ~0.75 μm associated with Fe<sup>2+</sup>-Fe<sup>3+</sup> charge transfer in cronstedtite and absorptions at ~0.95 μm and ~1.15 μm associated with octahedrally-coordinated Fe<sup>2+</sup> crystal field transitions. The Fe<sup>2+</sup> crystal field transitions in olivine (~1.05 and 1.3 μm) and the Fe<sup>2+</sup>-Fe<sup>3+</sup> intervalence charge transfer in magnetite (~1–1.3 μm) likely also contribute to this broad spectral feature. In

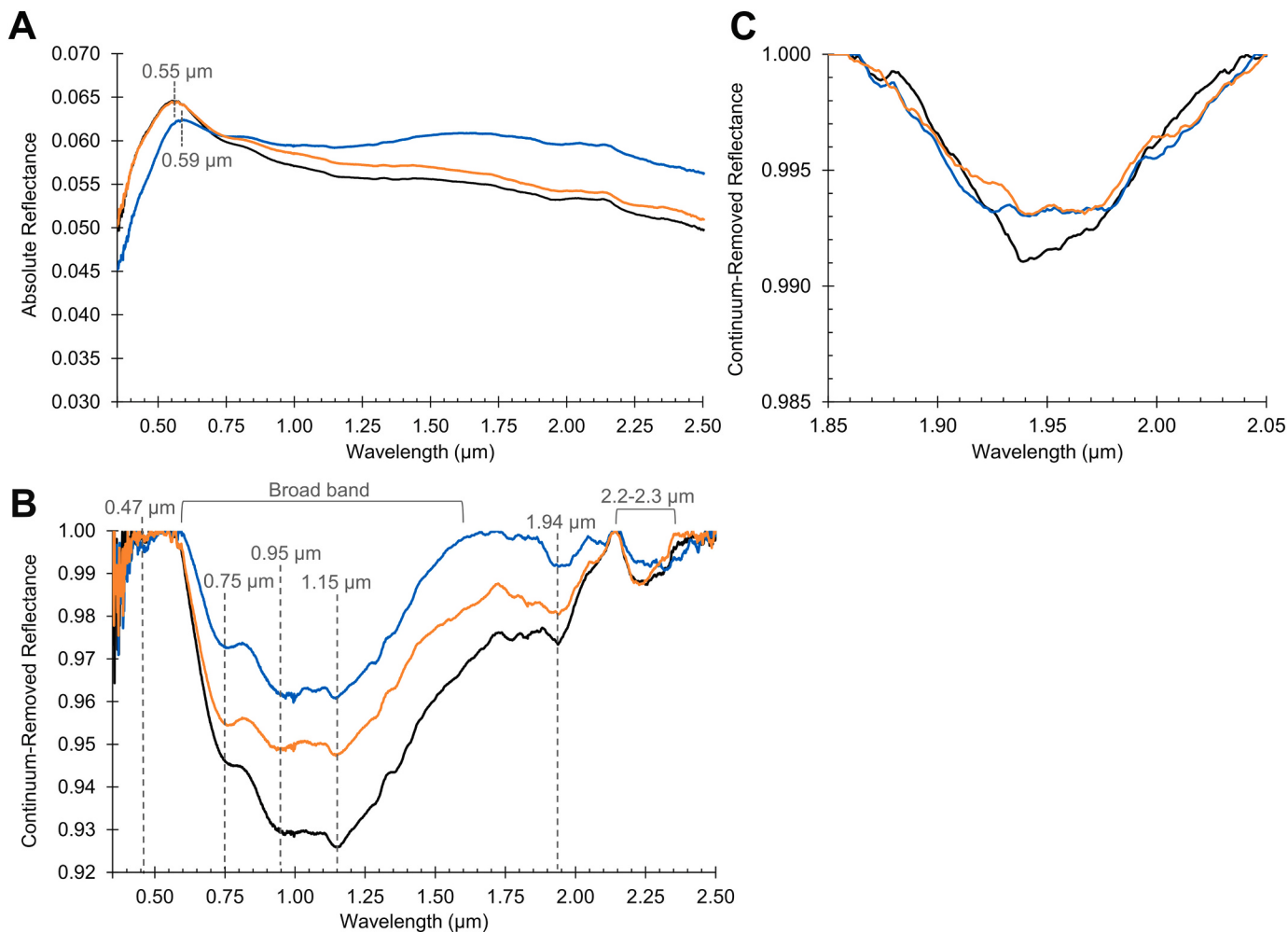


**Fig. 4.** Visible to near-infrared (VNIR; 0.35–2.5 μm) spectra of the unirradiated (black), H<sup>+</sup>-irradiated (orange), and He<sup>+</sup>-irradiated (blue) surfaces of the dry-cut Murchison slab. (A) Absolute reflectance versus wavelength of all three surfaces. Note the reddening and brightening of the He<sup>+</sup>-irradiated spectrum. (B) Continuum-removed reflectance spectra showing a broad band between ~0.6 and 1.6 μm made up of many minima including the ~0.75 μm, ~0.95 μm, and ~1.15 μm bands associated with Fe-bearing phyllosilicates. This broad band attenuates in response to both types of ion irradiation. (C) Continuum-removed spectra of the hydration band at ~1.95 μm largely resulting from adsorption of water under ambient data acquisition conditions. Note how the sharp feature in the unirradiated spectrum disappears after H<sup>+</sup>- and He<sup>+</sup>-irradiation. (For interpretation of the references to colour in this figure legend, the reader is referred to the web version of this article.)

**Table 1**

Reflectance and slope values for the unirradiated, H<sup>+</sup>-irradiated, and He<sup>+</sup>-irradiated samples. The average standard deviation of each spectrum is also reported.

	Unirradiated	H <sup>+</sup> -irradiated	He <sup>+</sup> -irradiated
Reflectance at 0.35 μm	4.98% ± 0.4%	5.02% ± 0.4%	4.52% ± 0.2%
Reflectance at 0.55 μm	6.46% ± 0.4%	6.45% ± 0.4%	6.18% ± 0.2%
Reflectance at 2.50 μm	4.98% ± 0.4%	5.10% ± 0.4%	5.63% ± 0.2%
Spectral slope from 0.65–2.5 μm (μm <sup>-1</sup> )	-0.0067	-0.0062	-0.0029

general, both He<sup>+</sup>- and H<sup>+</sup>-irradiation reduce these absorption band strengths, with He<sup>+</sup>-irradiation inducing greater attenuation, especially in the ~0.75 μm band. An absorption band also occurs between ~2.2–2.3 μm in the unirradiated, H<sup>+</sup>-irradiated, and He<sup>+</sup>-irradiated spectra which may represent metal-OH in matrix phyllosilicates and/or amorphous phases (Cloutis et al., 2011b, 2012). At shorter wavelengths,

the He<sup>+</sup>-irradiated spectrum includes an absorption at ~0.47 μm which may correspond to a presently undetermined Fe<sup>3+</sup>-bearing phase (e.g., Morris et al., 1985).

In addition, OH<sup>-</sup>/H<sub>2</sub>O hydration bands possibly associated with matrix phyllosilicates or another hydrated phase are present at ~1.95 μm (Fig. 4C) and ~1.40 μm (e.g., Bishop et al., 2017; Cloutis et al., 2012) in all three spectra. However, it is important to note that reflectance measurements were not performed under vacuum, so these water bands likely include a significant contribution from adsorbed water on the surface of the Murchison sample due to exposure to ambient air (e.g., Beck et al., 2010; Lantz et al., 2015; Takir et al., 2013). We also note that the ~1.95 μm absorption band in the unirradiated spectrum is sharp compared to the broad feature seen in the H<sup>+</sup>- and He<sup>+</sup>-irradiated spectra (Fig. 4C). Interestingly, Lantz et al. (2017) observed a similar sharp feature within the ~3 μm OH<sup>-</sup> stretching band (associated with Mg-rich phyllosilicates and adsorbed water) of their unirradiated Mighei, Alais, and Tagish Lake spectra which disappeared after He<sup>+</sup> and Ar<sup>+</sup> irradiation, making the absorption bands appear more broad. Band minima from Lantz et al. (2015, 2017) also shifted toward slightly longer wavelengths following ion irradiation.

### 3.3. Microprobe two-step laser-desorption mass spectrometry ( $\mu\text{L}^2\text{MS}$ )

Summed spectra and spatial maps generated using VUV photoionization (118 nm) were acquired from unirradiated,  $\text{H}^+$ -irradiated, and  $\text{He}^+$ -irradiated regions of Murchison (Fig. 5). As indicated by spectral comparisons (Fig. 5B and C), the overall shape of the mass envelopes remains largely unchanged after both types of ion irradiation. All the spectra show the characteristic 14 m/z periodicity that is due to alkylation series in which  $\text{R}-\text{H}$  is replaced by  $\text{R}-\text{CH}_2-\text{H}$ . Although chemical distribution maps (Fig. 5A) do not show a significant increase or decrease in organic content from  $\text{H}^+$ -irradiation, summed spectra suggest that  $\text{H}^+$ -irradiation increases the abundance of some low-molecular-weight free organic species (i.e., not bound as macromolecular assemblages), such as methanethiol, butane, glycolic acid, thiophene, cyclooctane, and naphthalene. While the bulk organic content is likely not changing, results suggest that  $\text{H}^+$ -irradiation cleaves macromolecular species ( $m/z > 10^6$ ), which cannot be thermally desorbed by the  $\mu\text{L}^2\text{MS}$  infrared laser, into smaller molecular fragments (i.e., free organic species), including polycyclic aromatic hydrocarbons (PAHs), that can be readily desorbed from the sample's surface and detected by the instrument. In contrast,  $\text{He}^+$ -irradiation causes a decrease in bulk organic content, as evidenced in both summed spectra and chemical distribution maps. Interestingly,  $\text{OH}^-$  ( $m/z \sim 17$  amu) and  $\text{H}_2\text{O}$  ( $m/z \sim 18$  amu) abundances increase after  $\text{H}^+$ - and  $\text{He}^+$ -irradiation.

### 3.4. Field-emission scanning transmission electron microscopy (FE-STEM)

#### 3.4.1. Matrix samples

**3.4.1.1.  $\text{He}^+$ -irradiated.** The  $\text{He}^+$ -irradiated matrix cross-section exhibits a highly vesiculated ion-affected region with an average thickness of  $\sim 100$  nm and maximum thickness of 130 nm (Fig. 6A). Vesicles are spherical and oblong in shape and can reach  $\sim 130$  nm in length. Complete amorphization of phyllosilicates (i.e., absence of lattice fringes, or atomic planes) extends to a depth of  $\sim 150$ –175 nm, consistent with findings from Keller et al. (2015b). In order of decreasing concentration, EDX analysis suggests that the ion-affected region consists of O, Si, Fe, Mg, Al, S, and Ni (Fig. 6C; Table 2). Potential Fe-bearing nanoparticles ( $\leq$  nm diameter) are present in isolated areas (Fig. 6B). Although some of these nanoparticles occur in the amorphous region below the vesiculated layer and even less within the vesiculated layer itself, most extend into the unaltered substrate.

**3.4.1.2.  $\text{H}^+$ -irradiated.** Ion irradiation effects in the  $\text{H}^+$ -irradiated matrix FIB-section show significant differences from the  $\text{He}^+$ -irradiated sample. The vesiculated layer is thinner, between 40 and 60 nm in thickness, and the vesicles are smaller, reaching up to  $\sim 50$  nm in width (Fig. 7A and B). Complete amorphization of matrix phyllosilicates extends 60–70 nm below the surface (Fig. 7C). The composition of this sample's ion-processed zone is similar to that of the  $\text{He}^+$ -irradiated

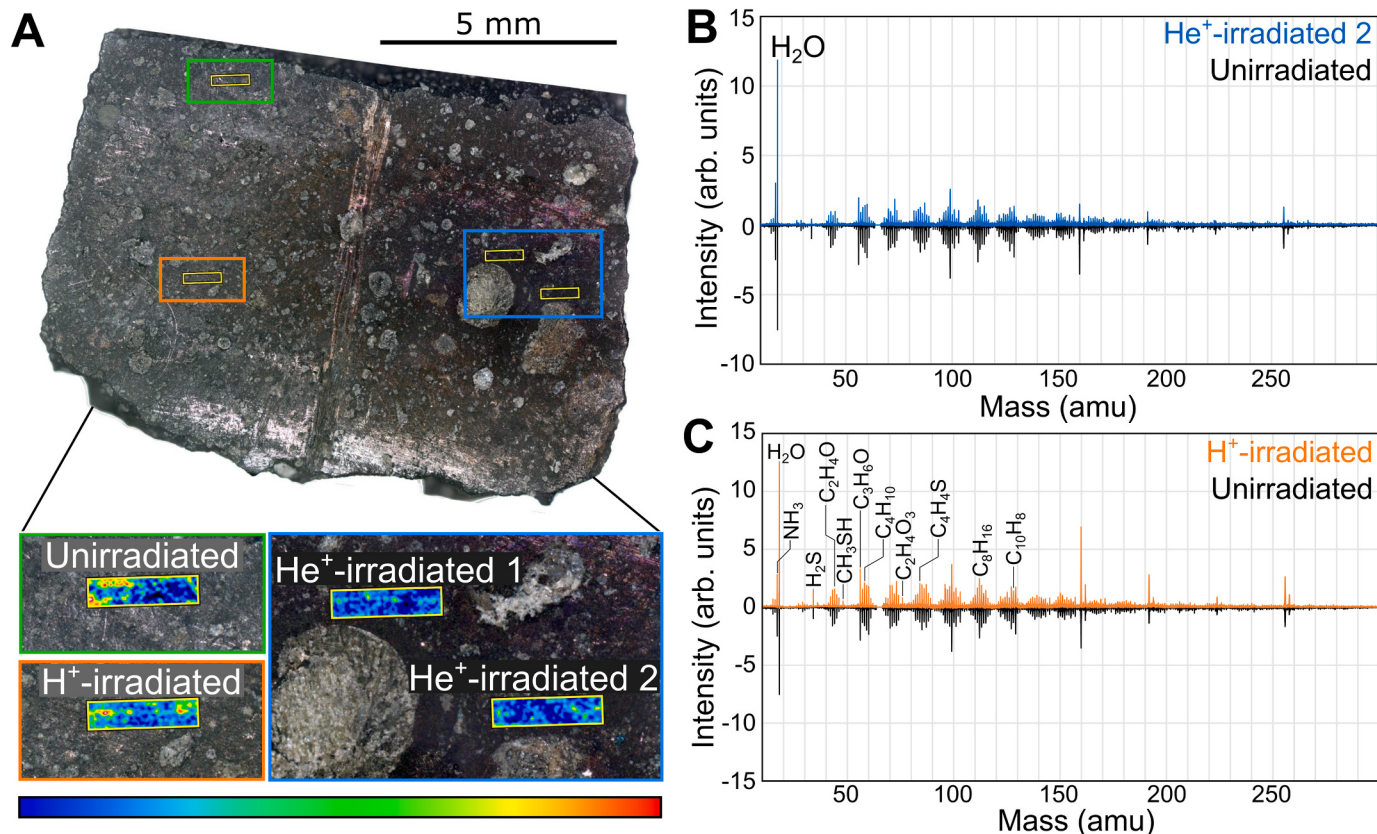


**Fig. 5.** Organic analyses of the Murchison surface by  $\mu\text{L}^2\text{MS}$  using vacuum ultraviolet photoionization (118 nm). (A) Chemical maps showing the abundance and spatial distribution of organic species in unirradiated (green box),  $\text{H}^+$ -irradiated (orange box), and  $\text{He}^+$ -irradiated (blue box) Murchison. The spectrum colormap portrays relative organic concentrations, with blue representing lower organic content and red representing higher organic content. (B) Normalized spectral comparison of  $\text{He}^+$ -irradiated (blue) and unirradiated (black) Murchison showing the mass envelope of organic species and the near uniform decrease in their abundance from  $\text{He}^+$ -irradiation. Interestingly,  $\text{H}_2\text{O}$  ( $m/z \sim 18$  amu) and  $\text{OH}^-$  ( $m/z \sim 17$  amu) contents increase following  $\text{He}^+$ -irradiation. (C) Normalized spectral comparison of  $\text{H}^+$ -irradiated (orange) and unirradiated (black) Murchison showing the mass envelope of organic species and an increase in some of their abundances from  $\text{H}^+$ -irradiation. Some species that increase in abundance are labeled. Like  $\text{He}^+$ -irradiation,  $\text{H}^+$ -irradiation also causes an increase in  $\text{H}_2\text{O}$  and  $\text{OH}^-$  content. (For interpretation of the references to colour in this figure legend, the reader is referred to the web version of this article.)

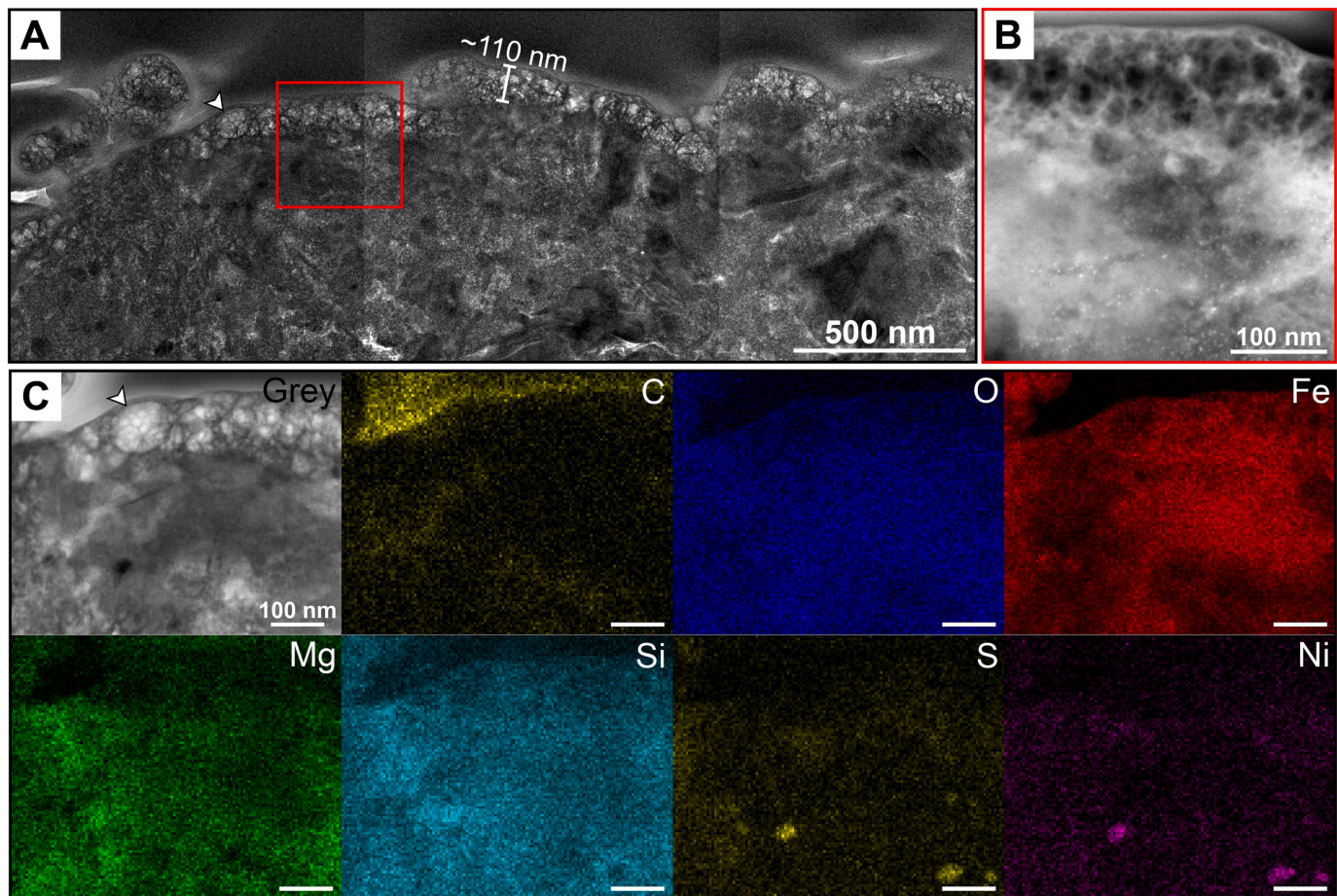


**Fig. 6.** TEM imaging and microanalysis of the  $\text{He}^+$ -irradiated matrix sample. (A) Conventional TEM mosaic showing the highly vesiculated,  $\sim 105 \text{ nm}$  thick (white bracket) region at the surface of the sample with heterogeneous, unaltered matrix material below. The white arrow identifies a region containing both small (5–50 nm) and large (120 nm) vesicles. (B) Small Fe-bearing nanoparticles (bright specks) in a HAADF STEM image of the area outlined in red in (A). (C) Qualitative EDX analysis of the area within the BF STEM image (top left) showing compositionally heterogeneous matrix material. C (yellow), O (blue), Fe (red), Mg (green), Si (cyan), S (yellow), and Ni (magenta) maps are shown. Note the ovoid S- and Ni-enriched grains. The white arrow indicates the same vesicles denoted in (A). (For interpretation of the references to colour in this figure legend, the reader is referred to the web version of this article.)

**Table 2**

Major results from the TEM and EDX analyses of the ion-affected regions investigated in this study (six FIB cross-sections). Arrows are used to indicate successive layers with depth.

Sample	Thickness	Vesiculation	Microstructure	Surface chemistry
$\text{He}^+$ -irradiated matrix	$\sim 160 \text{ nm}$	High	Completely amorphous	No change
$\text{H}^+$ -irradiated matrix	$\sim 65 \text{ nm}$	High	Completely amorphous	No change
$\text{He}^+$ -irradiated Mg-rich olivine	$\sim 75 \text{ nm}$	Moderate	Completely amorphous layer (uppermost $\sim 15 \text{ nm}$ ) → partially amorphous layer (lateral variation in extent of amorphization)	Si-enriched/Mg-depleted layer (upper 20–40 nm)
$\text{H}^+$ -irradiated Mg-rich olivine	50–85 nm	Moderate	Partially amorphous to completely polycrystalline (lateral variation)	Variable; Some regions have a thin, laterally discontinuous Si-enriched/Mg-depleted layer → Mg-enriched/Si-depleted layer ( $\sim 20$ –30 nm)
$\text{He}^+$ -irradiated Fe-rich olivine	120–180 nm	High	Completely amorphous	No change
$\text{H}^+$ -irradiated Fe-rich olivine	$\sim 65 \text{ nm}$	Low	Partially amorphous → completely amorphous → partially amorphous	Mg-Fe-enriched layer (2–5 nm) → discontinuous Si-enriched/Mg-Fe-depleted layer ( $\sim 10$ –20 nm) → Si content progressively decreases upward from base of ion-affected region

matrix sample, consisting of O, Si, Fe, Mg, S, Al, and Ni (again, in order of decreasing concentration) (Fig. 7D; Table 2). No nanoparticles were identified in the  $\text{H}^+$ -irradiated cross-section.

### 3.4.2. Mg-rich olivine samples

**3.4.2.1.  $\text{He}^+$ -irradiated.** Moderate vesiculation occurs in the  $\text{He}^+$ -irradiated Mg-rich olivine cross-section. The ion-affected region ranges between 65 and 85 nm in thickness. Vesicles are mostly irregular-oblong or ovoid in shape and range in size from 4 to 90 nm (Fig. 8A). HRTEM

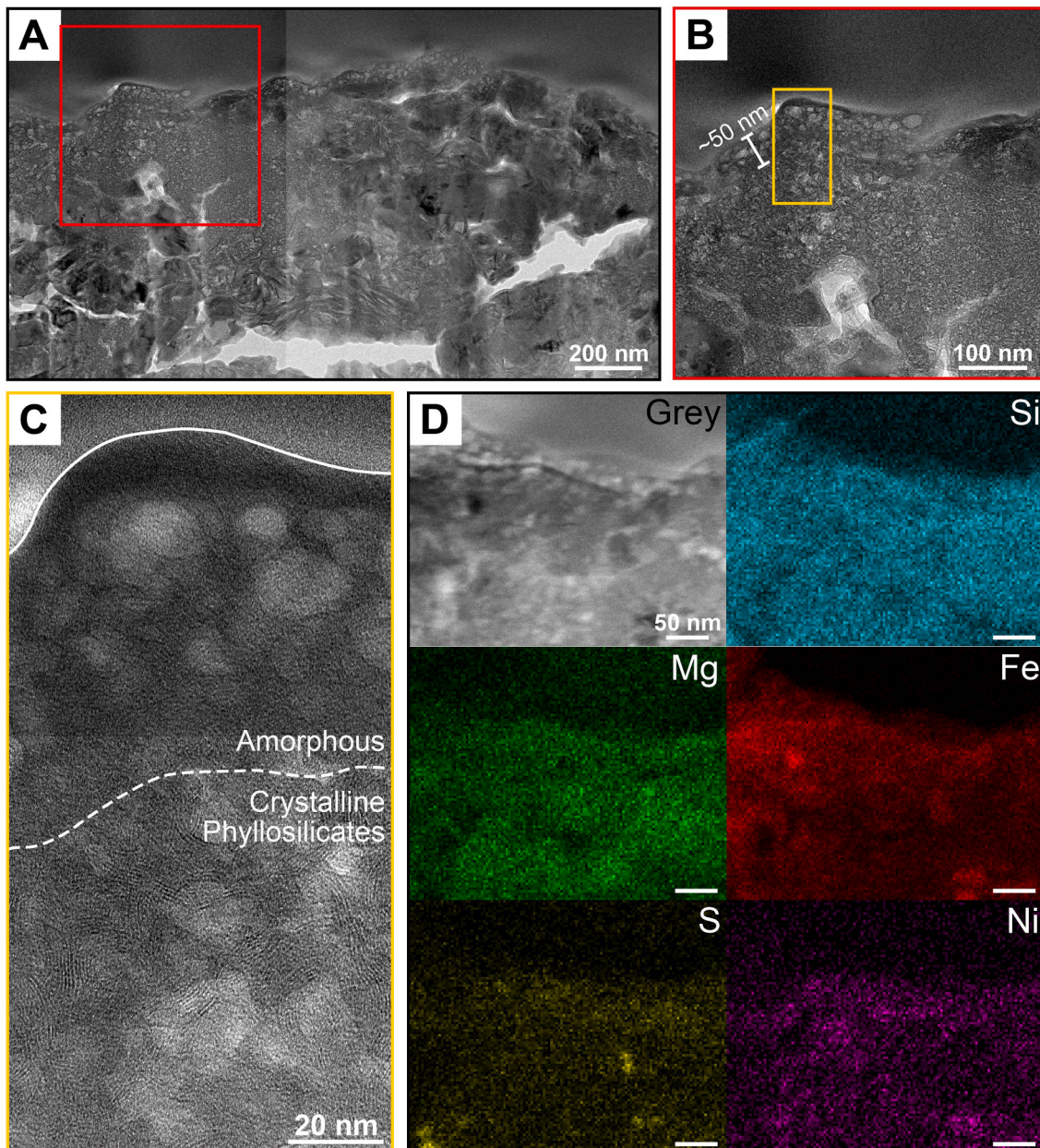


**Fig. 7.** TEM imaging and microanalysis of the  $\text{H}^+$ -irradiated matrix sample. (A) Conventional TEM mosaic showing the ion-affected region and heterogeneous nature of the underlying, unaltered matrix material. (B) Higher magnification conventional TEM image of the red box in (A). The thickness of the vesiculated region is indicated by the white bracket. (C) HRTEM stack from the region identified by the yellow rectangle in (B) showing a  $\sim 60\text{--}70\text{ nm}$  amorphization depth. The dashed line defines the boundary between amorphous and crystalline phyllosilicates. (D) Qualitative EDX map set including Si (cyan), Mg (green), Fe (red), S (yellow), and Ni (magenta) of the area within the BF STEM image (top left), confirming the heterogeneous composition of Murchison's matrix. (For interpretation of the references to colour in this figure legend, the reader is referred to the web version of this article.)

imaging reveals spatial variations in the relative abundances of amorphous versus crystalline material in the ion-affected region. As shown in Fig. 8B, in some areas, polycrystalline material dominates and can occur at the surface of the sample. However, in other regions, amorphous zones dominate, with polycrystalline material only occurring in isolated regions (Fig. 8C). In most areas, there is a thin ( $\sim 5\text{--}15\text{ nm}$ ), dark, mottled, structurally disordered layer at the base of the ion-affected region whose composition is consistent with the substrate. Some areas of the ion-affected region appear to have a completely amorphous layer in the uppermost  $\sim 15\text{ nm}$  (Fig. 8C), resembling the microstructure of  $\text{He}^+$ -irradiated olivine grains from previous studies (Bradley et al., 1996). Quantitative EDX maps and element intensity line profiles suggest the presence of a Si-enriched and Mg-depleted layer at the sample's

surface (Fig. 8D). However, the Si and Mg content in this layer and its thickness (20–40 nm) varies laterally within the sample (Table 2).

**3.4.2.2.  $\text{H}^+$ -irradiated.** The  $\text{H}^+$ -irradiated Mg-rich olivine cross-section contains many grain boundaries and includes domains of both forsterite and enstatite. The width of the ion-affected region varies between  $\sim 50$  and  $85\text{ nm}$ , and the microstructure of its lower boundary with the host crystalline grain is complex and gradational (Fig. 9A). The ion-affected region is moderately vesiculated with spherical, ovoid, and irregular vesicle morphologies ranging in size from  $<10\text{ nm}$  to  $80\text{ nm}$ . Variations in thickness and vesiculation within the ion-processed zone may result from differences in grain chemistry and crystallographic orientation relative to the ion beam. Unlike the completely amorphous

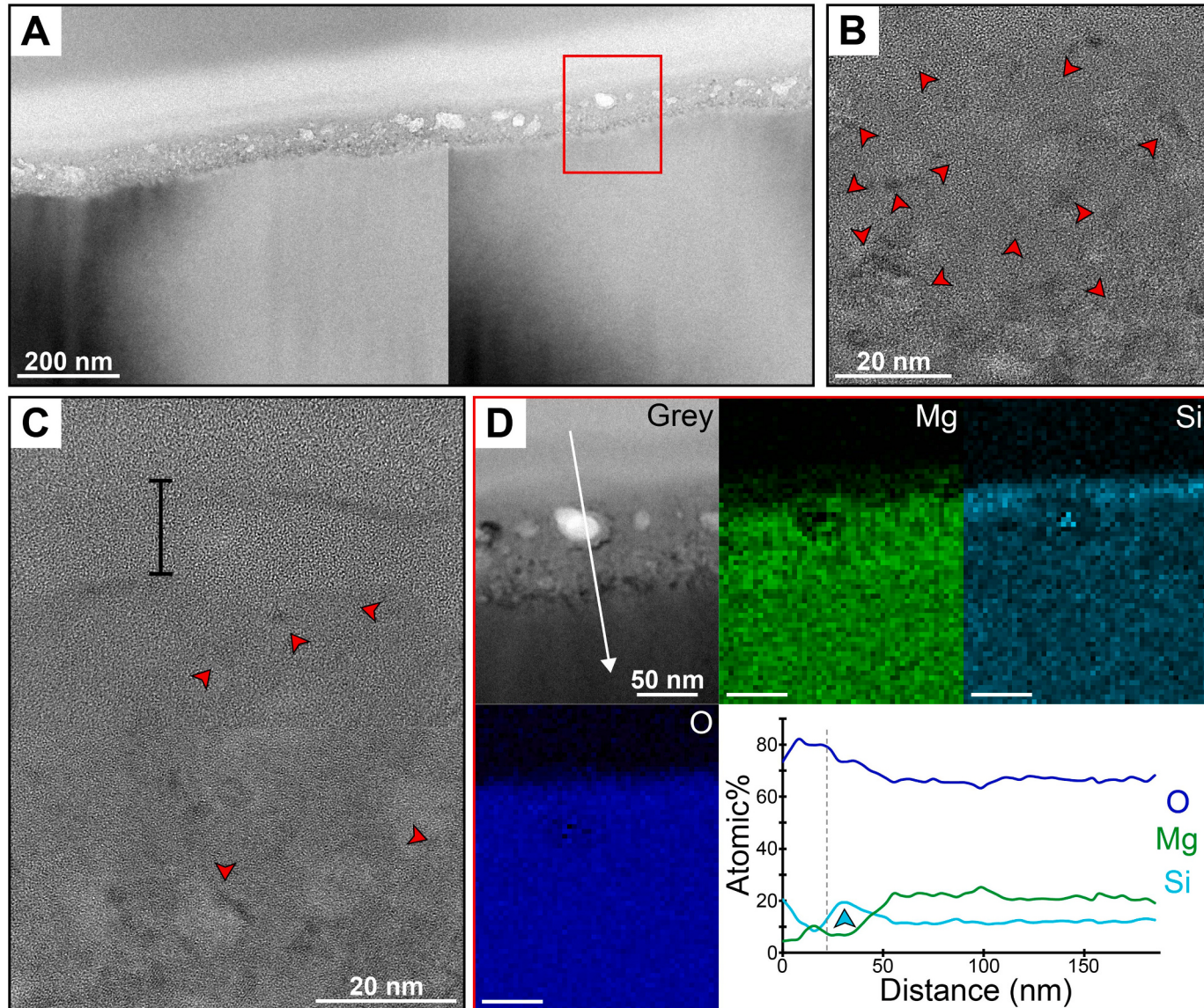


**Fig. 8.** TEM imaging and microanalysis of the  $\text{He}^+$ -irradiated Mg-rich olivine sample. (A) Conventional TEM mosaic showing the vesiculated ion-affected region. (B) HRTEM image of the ion-affected region showing both polycrystalline (red arrows) and amorphous material. (C) HRTEM stack of an ion-affected area dominated by amorphous material. The few polycrystalline regions are indicated by red arrows. Substrate lattice fringes are visible at the bottom of this image. The black bracket indicates a completely amorphous,  $\sim 15$  nm layer. (D) Quantitative EDX map set of the area bounded by the red box in (A). Mg is green, Si is cyan, and O is blue. A quantified elemental intensity profile (bottom right) extracted from the white arrow in the BF STEM image (top left) displays a slight Si-enrichment and Mg-depletion at the very surface of the sample. The cyan arrow indicates the Si-enriched region. The vertical dashed line indicates the top edge of the sample. (For interpretation of the references to colour in this figure legend, the reader is referred to the web version of this article.)

rim ( $\sim 25$  nm) observed in  $\text{H}^+$ -irradiated olivine by Bradley et al. (1996), this ion-affected region is predominantly polycrystalline with very few, isolated amorphous islands (Fig. 9B–D). Some areas of the sample contain no amorphous material within the ion-processed rim. When amorphization does occur, it tends to be located at depths shallower than  $\sim 40$  nm.

Quantitative EDX and elemental profile analysis indicate some variation in chemical trends across the sample surface. Specifically, a Mg-enriched and slightly Si-depleted region ( $\sim 20$ – $30$  nm in thickness) generally occurs at or near the surface. In some locations, this Mg-enriched region is overlain by a layer enriched in Si relative to Mg (Fig. 9E). In contrast, another region of the sample analyzed with EDX includes three distinct zones within the ion-processed region. From surface to interior, these include a: Si and Mg-depleted region ( $\sim 4$ – $14$  nm), Mg-enriched and Si-depleted region ( $\sim 40$ – $50$  nm), and Si-enriched and Mg-depleted region ( $> 20$  nm) (Table 2).

### 3.4.3. Fe-rich olivine samples

**3.4.3.1.  $\text{He}^+$ -irradiated.** Similar to the  $\text{He}^+$ -irradiated matrix cross-section, the ion-affected region of the  $\text{He}^+$ -irradiated Fe-rich olivine sample is highly vesiculated, completely amorphous, and ranges between 120 and 180 nm in thickness (Fig. 10A). Conventional diffraction-contrast TEM imagery shows that vesicles, which are spherical and oblong in shape, are segregated based on size with the smallest vesicles ( $\leq 20$  nm) concentrated in the lower  $\sim 20$ – $30$  nm of the vesiculated region, and the larger ( $> 20$  nm) vesicles occurring exclusively above this region (Fig. 10B). The largest of vesicles (80–140 nm in length) are predominantly oblong. Secondary electron images show blistering on the sample's surface (Fig. 10C) which correlates in size and shape to the vesicles observed in TEM analyses. A similar surface texture was observed on Fe-Mg-silicate grains in Itokawa dust particles (e.g., Matsumoto et al., 2014, 2015). The mottled boundary ( $\sim 5$ – $20$  nm) between

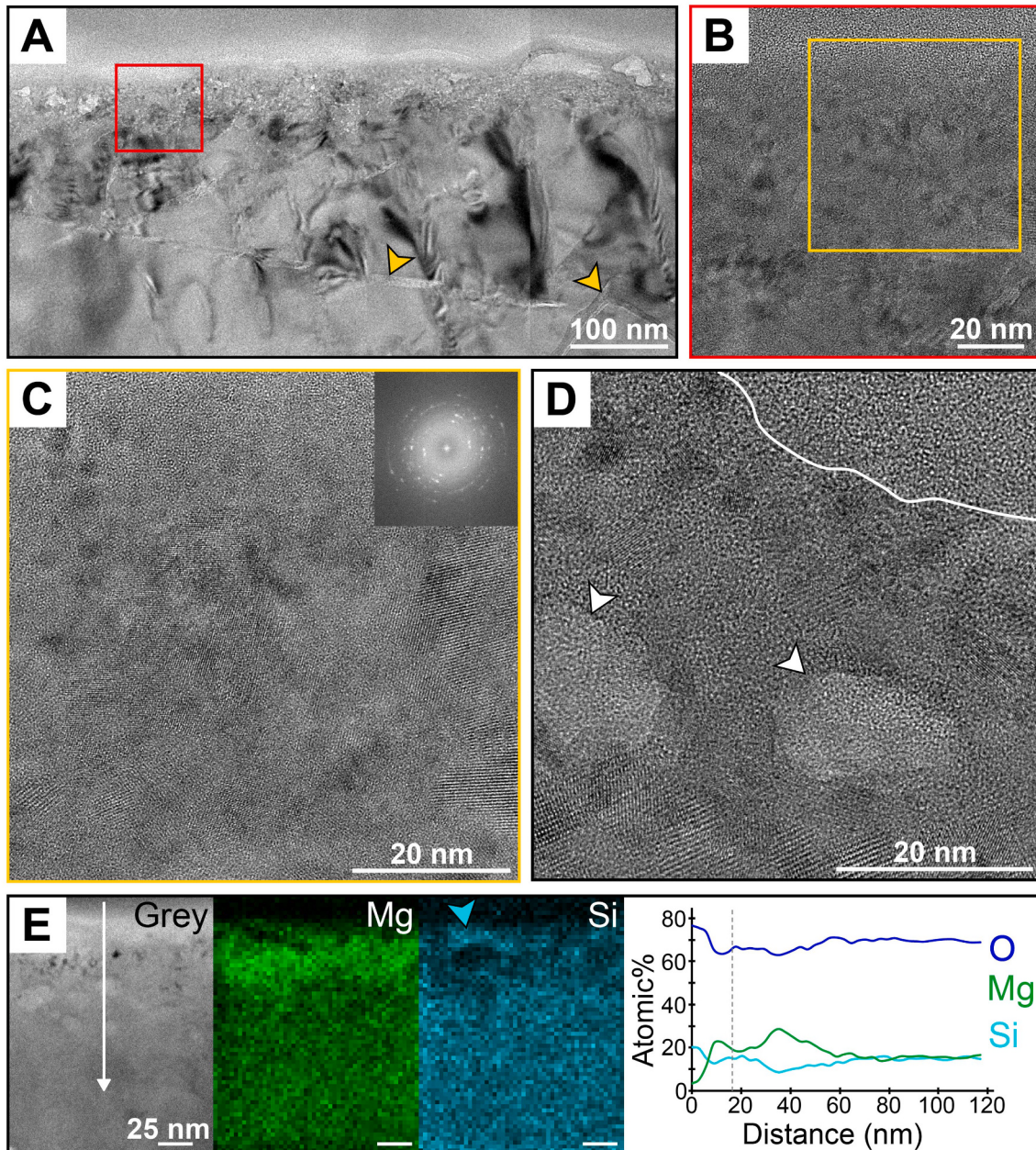


**Fig. 9.** TEM imaging and microanalysis of the  $\text{H}^+$ -irradiated Mg-rich olivine sample. (A) Conventional TEM mosaic showing the ion-affected region. Note the grain boundaries indicated by the yellow arrows. (B) HRTEM image of the area in the red box in (A). The ion-affected region is largely polycrystalline with amorphous islands. (C) A higher magnification HRTEM image of the yellow box in (B) showing lattice fringes. The inset FFT image confirms the nanocrystallinity in the ion-affected region. (D) HRTEM image showing that nanocrystallinity extends to the surface of the sample. Prominent vesicles (white arrows) surrounded by damaged olivine are also visible. (E) Quantitative EDX analysis (Mg in green, Si in cyan) of the region denoted by the BF STEM image (far left). A Mg-enriched, Si-depleted layer occurs at or near the surface of the sample. In some areas, Mg-enrichment is overlain by Si-enrichment at the surface (cyan arrow). A quantified elemental concentration profile (far right) extracted from the white arrow in the BF STEM image confirms these chemical trends. The vertical dashed line indicates the top edge of the sample. (For interpretation of the references to colour in this figure legend, the reader is referred to the web version of this article.)

the amorphous, vesiculated region and crystalline olivine substrate is also crystalline (Fig. 10D). No notable changes in chemistry were observed in the ion-affected region through qualitative and quantitative EDX analysis (Fig. 10E; Table 2).

**3.4.3.2.  $\text{H}^+$ -irradiated.** The  $\text{H}^+$ -irradiated Fe-rich olivine sample exhibits minor vesiculation and has an ion-affected region that is  $\sim 60\text{--}75$  nm thick (Fig. 11A). The vesicles vary in shape (spherical, oblong, and irregular) and have major axes that are consistently  $<25$  nm. HRTEM images and EDX analysis indicate the presence of three microstructurally and chemically distinct zones in the ion-affected region

(Fig. 11B and C). Zone 1 (outermost 2–5 nm) is a laterally discontinuous layer showing a mottled, structurally disordered, and mostly amorphous microstructure that is comparatively enriched in Mg and Fe and depleted in Si.

Zone 2 is characterized by a  $\sim 10\text{--}20$  nm thick, completely amorphous, discontinuous layer with highly undulating upper and lower boundaries. This layer is enriched in Si and depleted in Mg and Fe. Si content in this region, compared to the olivine substrate, varies: sometimes its Si content is higher, sometimes lower, and sometimes its approximately the same as the substrate.

Zone 3 contains the bulk of the ion-affected material ( $\sim 40\text{--}60$  nm

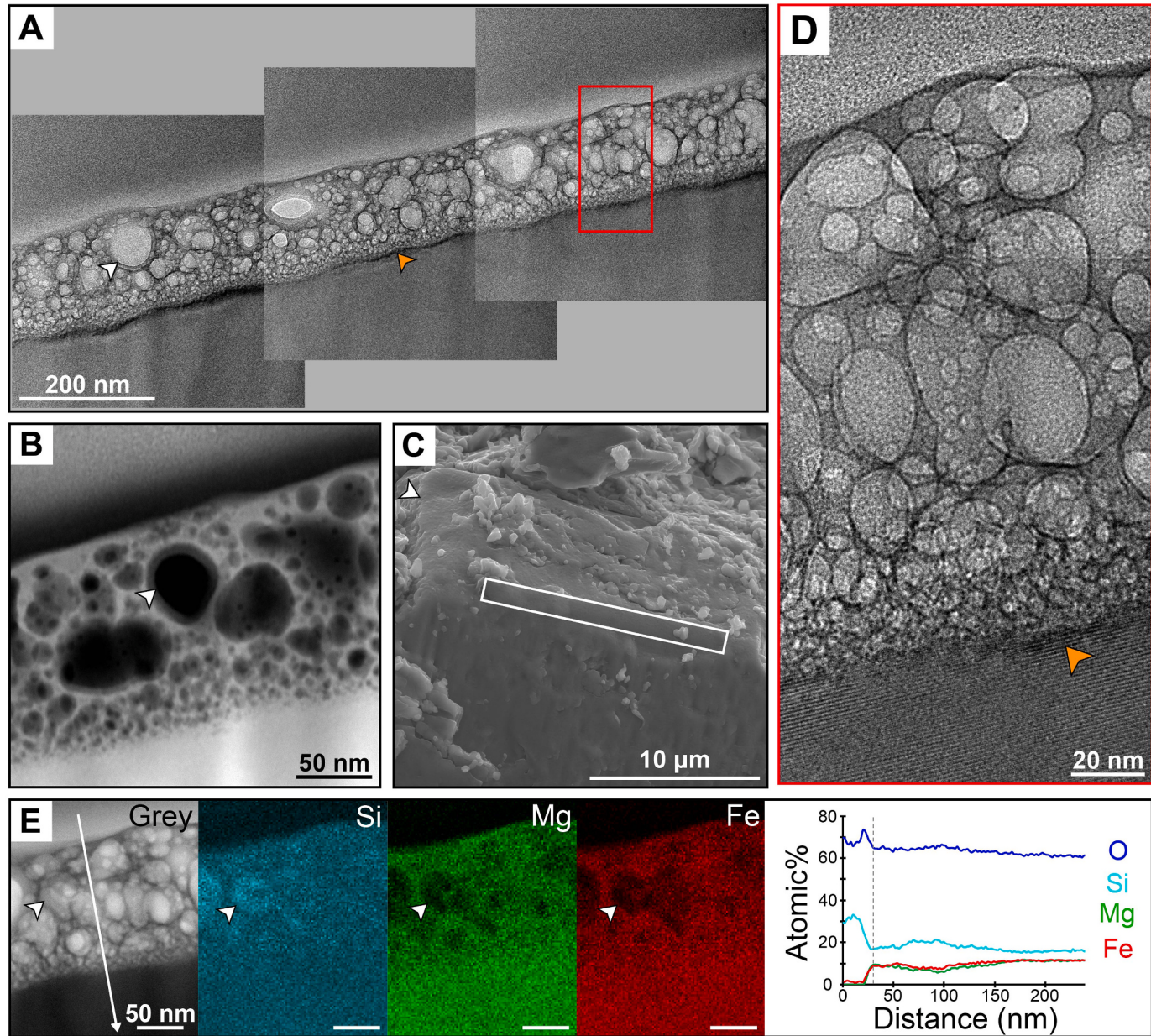


**Fig. 10.** TEM imaging, STEM imaging, and microanalysis of the  $\text{He}^+$ -irradiated Fe-rich olivine sample. (A) Conventional TEM mosaic showing the highly vesiculated ion-affected region. The white arrow indicates a vesicle and the orange arrow indicates the mottled, highly strained boundary layer between the vesiculated/amorphous and crystalline regions. (B) HAADF STEM image. Vesicles are now black (white arrow). No Fe-bearing nanoparticles are present. (C) A secondary electron image showing a bumpy, or blistered, surface texture on the olivine grain resulting from vesiculation. (D) HRTEM stack of the region outlined in red in (A) highlighting the boundary between the vesiculated/amorphous ion-affected region and crystalline olivine substrate. (E) Quantitative EDX analysis (Si in cyan, Mg in green, Fe in red) of the region denoted by the BF STEM image (far left). White arrows indicate the same vesicle in the Si, Mg, and Fe maps, respectively. A quantified elemental concentration profile (far right) extracted from the white arrow in the BF STEM image shows that no elemental enrichments or depletions occur in the ion-affected region of this olivine grain. The vertical dashed line indicates the top edge of the sample. (For interpretation of the references to colour in this figure legend, the reader is referred to the web version of this article.)

thick). Digital FFT diffractograms of HRTEM lattice fringe images are consistent with a mixture of amorphous olivine and polycrystalline islands. These polycrystalline islands are likely recrystallized olivine as indicated by the presence of randomly-oriented lattice fringes. Here, the Si content continuously decreases upward from the base of the ion-affected region. In some areas of this layer, Mg and Fe are slightly concentrated in the uppermost  $\sim 15\text{--}25\text{ nm}$ . Also of note is the mottled contrast of Zone 3, containing lighter and darker areas. Quantitative EDX analysis suggests the lighter areas correspond to a higher Si content while the darker regions correspond to higher Mg and Fe content (Table 2). Together, these zones resemble layers observed in some

Itokawa olivine and low-Ca pyroxene grains (Noguchi et al., 2014a, 2014b; Thompson et al., 2014).

#### 4. Discussion

We identified changes in the spectral, microstructural, and chemical properties of the Murchison meteorite in response to ion irradiation. Similarities and differences between our samples, other experimental ion irradiation studies, and analyses of lunar and Itokawa returned samples are discussed in detail below. We also discuss the effect of ion irradiation on two important volatile phases in carbonaceous asteroids:

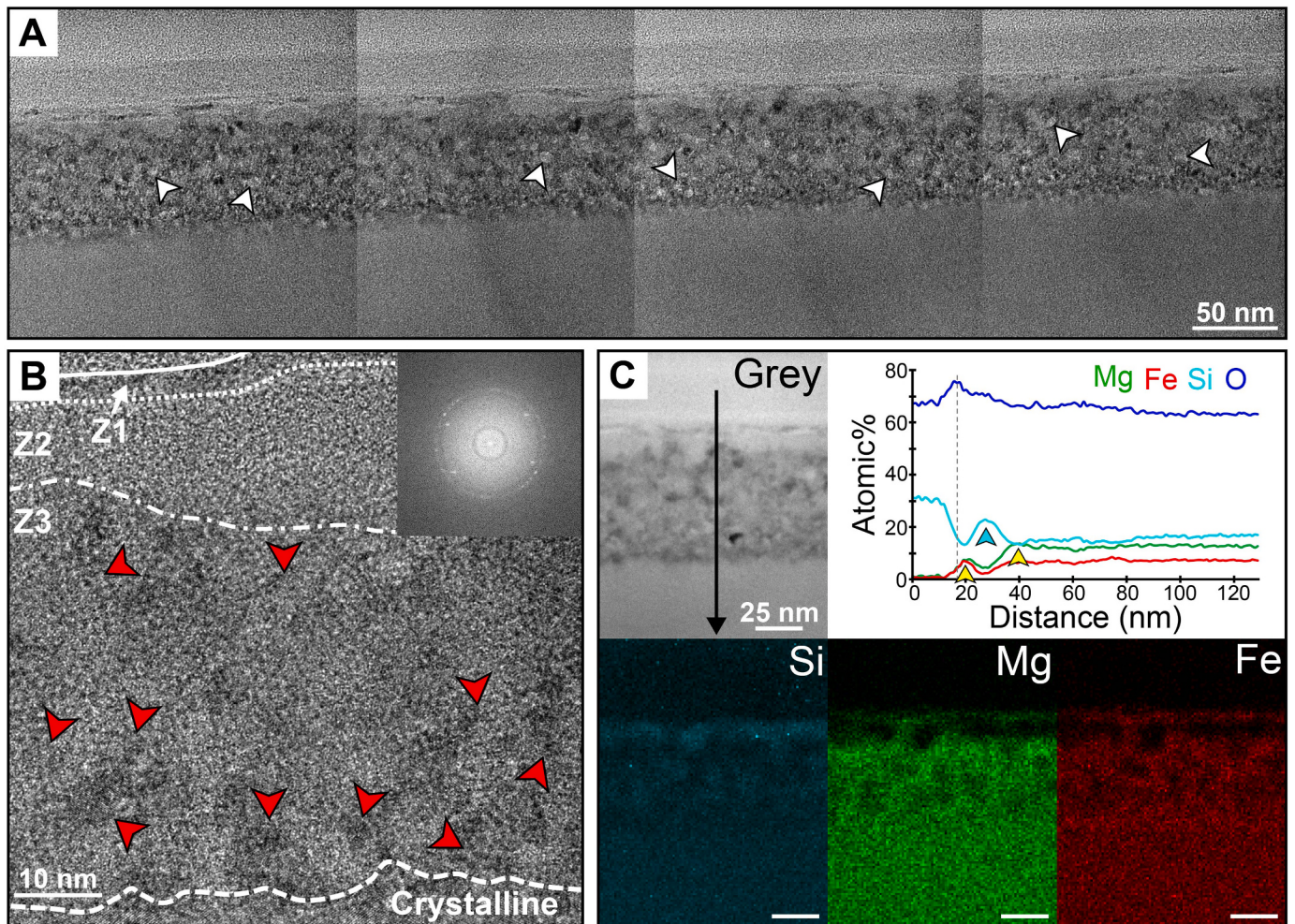


**Fig. 11.** Conventional TEM imaging and microanalysis of the  $\text{H}^+$ -irradiated Fe-rich olivine sample. (A) Conventional TEM mosaic showing the microstructure and depth of the ion-affected region. White arrows label small vesicles. (B) HRTEM image of the ion-affected region showing three microstructural zones (labeled Z1, Z2, and Z3). Polycrystalline ‘islands’ (indicated by red arrows) in zone 3 are surrounded by amorphous material. The inset FFT image (taken of the entire HRTEM image) supports the polycrystalline nature of the ion affected region. (C) Quantitative EDX map set of the region denoted by the BF STEM image (upper left). Si is shown in cyan, Mg in green, and Fe in red. A few nanometers below the sample’s surface, there is a ~10–20 nm thick Si-enriched and Mg-Fe-depleted layer. A quantified elemental concentration profile (top right) extracted from the black arrow in the greyscale image confirms this and other chemical trends. The cyan arrow denotes the Si-enriched region. The yellow arrows denote enrichments in Mg and Fe just above and below the Si-enriched layer. The vertical dashed line indicates the top edge of the sample. (For interpretation of the references to colour in this figure legend, the reader is referred to the web version of this article.)

carbon and water.

#### 4.1. Spectral changes

Differences in the slope, albedo, and absorption band strength of the unirradiated,  $\text{H}^+$ -irradiated and  $\text{He}^+$ -irradiated VNIR spectra represent the physical and chemical changes caused by ion irradiation. Slope reddening is observed in the spectra for both the  $\text{H}^+$ - and  $\text{He}^+$ -irradiated regions, with  $\text{He}^+$ -irradiation causing more significant reddening. Lantz et al. (2015) observed very minor reddening in their 40 keV  $\text{He}^+$ -irradiated Murchison sample, a variation which was smaller than those resulting from differences in viewing geometry, sample heterogeneity, and grain size. In previous ion irradiation studies, slope reddening was associated with metallization of iron and formation of  $\text{npFe}^0$  in the ion-processed samples (e.g., Hapke, 2001; Loeffler et al., 2009). Our high-resolution XPS analyses show surface reduction of  $\text{Fe}^{3+}$  and  $\text{Fe}^{2+}$  to  $\text{Fe}^0$  by  $\text{H}^+$ -irradiation and, thus, may support  $\text{npFe}^0$  production as the mechanism behind the slope reddening observed in this study. However, TEM analyses did not identify significant concentrations of  $\text{npFe}^0$  particles in the olivine or  $\text{H}^+$ -irradiated matrix cross-sections. Only the  $\text{He}^+$ -irradiated matrix sample contained nanoparticles, an observation which

is consistent with the stronger reddening trend in the  $\text{He}^+$ -irradiated spectrum (Fig. 4A). However, the fact that many nanoparticles in this sample were observed at depths exceeding the 4 keV  $\text{He}^+$  penetration range suggests that these nanoparticles may be intrinsic to the sample rather than ion-irradiation products. Thus, reddening in the  $\text{He}^+$ -irradiated spectrum may be predominantly driven by a different mechanism.

The absence of Fe-bearing nanoparticles in our Mg-rich olivine samples is unsurprising given that previous ion irradiation studies of Fe-poor minerals did not display the typical spectral reddening associated with  $\text{npFe}^0$  formation (Hapke, 1973; Yin et al., 1976). In contrast, the lack of nanoparticles in our Fe-rich olivine samples, where  $\text{Fe}^{2+}$  is available for reduction by ion irradiation, was unexpected. It is possible that minor production of  $\text{npFe}^0$  may still be occurring in Fe-rich olivine grains and  $\text{H}^+$ -irradiated matrix material, but these particles may not have been sampled by our extracted FIB sections. This unsampled  $\text{npFe}^0$  population could account for the slight reddening observed in the  $\text{H}^+$ -irradiated VNIR spectrum. The apparent absence of nanoparticles in our samples also may suggest that solar wind irradiation alone is not solely responsible for producing  $\text{npFe}^0$  on airless surfaces. Similar to what has been proposed by other studies (e.g., Glotch et al., 2015; Hood and

Schubert, 1980; Kramer et al., 2011), solar wind irradiation may provide the first step in nanoparticle formation by providing hydrogen to reduce native  $\text{Fe}^{2+}$  to  $\text{Fe}^0$ , while micrometeoroid impacts provide the thermal input to complete the process, although such a hypothesis cannot be confirmed by this study alone.

Another possibility is that spectral reddening may reflect a mineralogical change from crystalline phyllosilicates to more  $\text{Fe}^{2+}$ -rich amorphous material produced by ion irradiation-driven reduction of surface Fe, as indicated by our XPS analyses. Cloutis (2015) showed that synthetic lunar analog glasses with higher  $\text{Fe}^{2+}$  content exhibit a redder VNIR slope compared to more  $\text{Fe}^{3+}$ -rich glass. In support of this idea, by using electron energy loss spectroscopy (EELS), Keller et al. (2015a, 2015c) observed a higher  $\text{Fe}^{2+}/\text{Fe}^{3+}$  redox ratio in the amorphous, ion-affected rim of Murchison matrix material irradiated with 4 keV  $\text{He}^+$  compared to the unaltered substrate below. The more pronounced spectral reddening of the  $\text{He}^+$ -irradiated spectrum may also result from the removal of organic material by fragmentation and sputtering of macromolecular insoluble organic material (IOM), which tends to be slightly blue-sloped or flat longward of  $\sim 0.8\text{--}1.1 \mu\text{m}$  (Cloutis et al., 2011a, 2011b). However, IOM exhibits significant structural, compositional, and textural heterogeneity which makes it difficult to characterize IOM with a single, universal VNIR spectral signature (e.g., Blanco et al., 1988; Cloutis et al., 2011b; Draine, 1985; Johnson and Fanale, 1973; Rouleau and Martin, 1991). It is important to note that this study's spectral reddening trend contrasts with the bluing trend observed in ion-irradiated serpentine (Nakauchi et al., 2021) and spectral flattening observed in ion-irradiated pure bitumen samples (Moroz et al., 2004). The former difference is especially interesting considering serpentines dominate Murchison's mineralogy and suggests that ion irradiation of heterogeneous carbonaceous materials results in complex and even conflicting spectral changes.

Brightening observed in the long wavelength region ( $>\sim 0.75 \mu\text{m}$ ) of the  $\text{He}^+$ -irradiated spectrum (Fig. 4A) differs from the typical darkening-effect caused by space weathering of lunar and S-type asteroid/ordinary chondrite materials (e.g., Hapke, 2001) and the minor darkening observed at all VNIR wavelengths in a previously  $\text{He}^+$ -irradiated (40 keV) Murchison sample (Lantz et al., 2015). This brightening may be explained by ion-induced surface roughness, sample heterogeneity, and/or depletion of carbon (Dukes et al., 2015; Matsuoka et al., 2020; Moroz et al., 2004; Thompson et al., 2019, 2020; Vernazza et al., 2013). The roughening of a surface results in a higher proportion of diffusive versus specular reflection, increasing the apparent albedo. The formation of vesicles by  $\text{H}^+$  and  $\text{He}^+$  implantation likely contributes to this increase in surface roughness. Sample heterogeneity, specifically the proportion of chondrules in each irradiated region, also may account for the brightening observed in the  $\text{He}^+$ -irradiated spectrum. Chondrules, which constitute a larger portion of the  $\text{He}^+$ -irradiated region compared to the  $\text{H}^+$ -irradiated region, are optically brighter than matrix material. As suggested by Dukes et al. (2015), the removal of surface carbon may also contribute to the brightening trend, especially for the  $\text{He}^+$ -irradiated region whose  $\mu\text{L}^2\text{MS}$  data indicates a reduction in bulk organic carbon content. However, because carbonaceous material exhibits low reflectance over the whole VNIR wavelength range (e.g., Cloutis et al., 2011a, 2011b; Hendrix et al., 2016), removal of carbon-bearing species should result in brightening at all wavelengths. Considering this study only observes brightening longward of  $\sim 0.75 \mu\text{m}$  in the  $\text{He}^+$ -irradiated spectrum, carbon removal is, most likely, just one process contributing to albedo changes in VNIR spectra; a combination of concurrent effects from surface roughness, compositional heterogeneity, chemical reduction of iron, and carbon depletion are likely at play.

We also want to note that, while vesiculation is a common microstructural texture observed in experimentally ion irradiated (and laser irradiated) materials, the effect of vesiculation on the spectral albedo, slope, and contrast of these samples is poorly understood. The optical effect of vesiculation may be particularly relevant for ion irradiation experiments that create highly vesiculated surface textures, such as

those observed in matrix material from this study's Murchison sample (see Section 4.2.2 below for a microstructural discussion of vesiculation). A few studies have investigated the optical impact of vesicles in the thermal infrared spectra of terrestrial samples (e.g., obsidian vs. pumice, massive basalt vs. vesiculated basalt) (Carter et al., 2009; Ondrusek et al., 1993; Ramsey and Fink, 1999; Rost et al., 2018). These studies showed that vesiculated rocks exhibit reduced spectral contrast and lower reflectance compared to their massive counterparts, likely as a result of multiple scattering within vesicles (i.e., the cavity effect). However, vesicles in terrestrial igneous rocks are typically larger than those generated from ion irradiation experiments, the latter of which reach maximum lengths/radii of no more than  $\sim 100 \text{ nm}$  in our irradiated Murchison sample. Porosity's effect on airless regolith spectral signatures has been more extensively studied (e.g., Hapke, 2008; Kagawa et al., 2020; Kar et al., 2016, 2021; Kiuchi and Nakamura, 2014; Sakai and Nakamura, 2005), but, considering the definition of porosity (i.e., void space between spherical particles) is different from that of vesiculation (i.e., void space within coherent material), additional investigations examining the optical effects of nanometer-scale vesiculation, in particular, are needed to accurately interpret reflectance spectra of experimentally space-weathered materials.

Although  $\text{He}^+$ -irradiation induces greater attenuation, both types of ion irradiation reduce the spectral contrast of the broad absorption band between  $\sim 0.6$  and  $1.6 \mu\text{m}$  (Fig. 4B), the envelope of bands associated with  $\text{Fe}^{3+}$  and  $\text{Fe}^{2+}$  in serpentine group minerals, olivine, and possibly magnetite (Cloutis et al., 2011b, 2012). This observed change in absorption strength likely reflects the decomposition of olivine and phyllosilicates—the latter of which volumetrically dominates Murchison matrix material (Bland et al., 2004; Zolensky et al., 1993)—the chemical reduction of surface  $\text{Fe}^{3+}$  and  $\text{Fe}^{2+}$  to  $\text{Fe}^0$ , and subsequent formation of amorphous (i.e., glassy), Fe-bearing material in ion-irradiated regions. As mentioned previously, our high-resolution XPS data shows that a small amount of  $\text{Fe}^{3+}$  and  $\text{Fe}^{2+}$  in oxides, phyllosilicates, and olivine is reduced to metallic Fe. Although we did not acquire high-resolution XPS data from our  $\text{He}^+$ -irradiated region, it is likely that the formation of metallic Fe by chemical reduction is also occurring in this region, possibly to a greater extent due to the higher mass, energy, and penetration depth of the incident 4 keV  $\text{He}^+$  ions. Additionally, the Fe-bearing, amorphous (i.e., glassy) material resulting from phyllosilicate amorphization in ion-irradiated rims, which occurs to a greater depth in matrix regions irradiated with  $\text{He}^+$ , also may contribute to changes in spectral absorptions. Previous studies have shown that, compared to crystalline phases of similar composition, VNIR spectra of Fe-bearing glasses have broad absorptions with centers that can occur at slightly longer wavelengths (Cannon et al., 2017; Cloutis, 2015; Cloutis et al., 2008; Hapke, 2001; Moroz et al., 2014). For our spectra, broadening of the  $\sim 2.2\text{--}2.3 \mu\text{m}$  band occurs in the  $\text{He}^+$ -irradiated spectrum, but not the  $\text{H}^+$ -irradiated spectrum. Additionally, the sharp  $\sim 1.95 \mu\text{m}$  hydration band in our unirradiated spectrum disappeared following both types of ion irradiation—a phenomenon which has been previously associated with preferential sputtering of Mg and/or preferential amorphization of Mg-rich silicates (Lantz et al., 2015). Amorphous materials also exhibit a more gradually sloping UV wavelength signature ( $\sim 200\text{--}400 \text{ nm}$ ) owing to a wide variation in their metal-O bond distances (Cloutis et al., 2008). Such a feature is not present in our  $\text{H}^+$ - or  $\text{He}^+$ -irradiated VNIR spectra. However, spectral effects from Fe-bearing amorphous material in our samples may be overprinted by stronger signatures associated with unaltered crystalline phyllosilicates and olivine. Finally, while the addition of optically opaque phases (e.g.,  $\text{npFe}^0$ , magnetite, organics) is known to weaken spectral absorption bands in naturally and experimentally space-weathered materials and meteorites (e.g., Cloutis et al., 2011a, 2011b, 2012; Hapke, 2001; Pieters and Noble, 2016 and references therein), such phases cannot be attributed to the reduction in spectral contrast observed in this study with certainty, for potential Fe-bearing particles were only observed in one sample analyzed with TEM, as noted previously.

Together, this study's spectral results, which generally suggest that He<sup>+</sup>-irradiation of Murchison causes reddening and brightening in the longer wavelength region, are particularly interesting when put into context of space weathering on target asteroids Bennu and Ryugu. Recent spectral analysis of Bennu indicates that space weathering leads to brightening and bluing of initially red fresh material (DellaGiustina et al., 2020). Brightening first occurs in the near-ultraviolet wavelength region while further space weathering progressively brightens the visible to near-infrared wavelength region, yielding a moderately blue slope, overall, on Bennu. In contrast, spectral analysis of Ryugu suggests that initially blue fresh material reddens over time, and one possible cause of this reddening trend is space weathering (Morota et al., 2020). While other processes like solar heating may also contribute to the spectral properties of asteroids (especially Ryugu), when considered together, the spectral results discussed above corroborate a key finding from previous experimental space weathering studies of carbonaceous materials—that carbonaceous asteroids likely do not undergo lunar-style space weathering (e.g., Lantz et al., 2013; Thompson et al., 2019, 2020).

#### 4.2. Microstructural changes

Overall, the ion-irradiated regions evaluated in this study exhibit a variety of microstructural and chemical alterations in response to ion-irradiation that are consistent with signatures of solar wind exposure in returned samples (Table 2). Microstructural features observed in H<sup>+</sup>- and He<sup>+</sup>-irradiated Murchison cross-sections include amorphization, nanocrystallinity, and vesiculation. However, TEM imaging shows that ion-irradiation induced microstructural changes are not consistent across mineral phases. Olivine samples exhibit varying degrees of vesiculation and structural disorder. The 4 keV He<sup>+</sup> ions, which have a larger mass, kinetic energy, and stopping power than 1 keV H<sup>+</sup>, are capable of displacing more atoms through nuclear elastic collisions and, thus, are expected to cause more pronounced physical, chemical, and structural modifications.

##### 4.2.1. Rim thickness and amorphization

At low kinetic energies (i.e., keV), like those employed in this study, incident light ions (e.g., H<sup>+</sup> and He<sup>+</sup>) lose their energy via both electronic (inelastic) and nuclear (elastic) collisions in similar proportions, where the nuclear component causes target atoms to be permanently displaced from their lattice positions (Johnson, 1990). Complete amorphization occurs once these atomic displacements reach a critical concentration, which can vary from material to material. Ultimately, incident ions are either scattered out of the target or lose all their kinetic energy and come to rest (i.e., are implanted) in the sample (e.g., Carrez et al., 2002; Johnson, 1990; Sigmund, 1981).

Thicknesses of ion-affected surface layers in experimentally-irradiated phases typically correlate with the penetration depth (i.e., range) of incident implanted ions in the sample. (Although, the atomic displacement damage reaches a maximum at a slightly shallower depth than the maximum penetration range.) As mentioned in section 2.6, we used SRIM to model ion range and damage in serpentine (proxy for Murchison matrix material), Mg-rich olivine, and Fe-rich olivine. For the samples and irradiation conditions presented here, SRIM calculations indicate a maximum implantation depth for 1 keV H<sup>+</sup> and 4 keV He<sup>+</sup> in olivine of ~35 nm and ~70 nm, respectively. Both ions penetrate to greater depths of ~50 nm and ~80 nm, respectively, in serpentine because of its lower atomic density. As noted, the atomic displacement (damage) depths are generally 10–20% less than the corresponding implantation depth. While SRIM calculations by no means perfectly model ion damage or implantation profiles, they provide a point of comparison to investigate substrate properties that may be affecting ion-surface interactions.

Only the He<sup>+</sup>-irradiated Mg-rich olivine sample (Fig. 8) has an ion-processed zone whose thickness is roughly consistent with SRIM

calculations. Both the vesiculated layer thickness and amorphization depth of the H<sup>+</sup>- and He<sup>+</sup>-irradiated matrix samples exceeds SRIM estimates by approximately 30% and 80% respectively (Figs. 6 and 7). The H<sup>+</sup>-irradiated Mg-rich olivine (Fig. 9), He<sup>+</sup>-irradiated Fe-rich olivine (Fig. 10), and H<sup>+</sup>-irradiated Fe-rich olivine (Fig. 11) samples also have thicker ion-processed zones than what was predicted by SRIM. Interestingly, the depth of the amorphous layer in the H<sup>+</sup>-irradiated Fe-rich olivine sample corresponds to the maximum atomic displacement depth estimated by SRIM (5–12 nm) (Fig. 11). It should be noted that porosity increases ion implantation depths, particularly for the matrix cross sections. Thus, it is expected that porous matrix material in meteorites would exhibit deeper ion implantation and damage compared to the non-porous serpentine mineralogy employed in the SRIM code (Keller et al., 2015b). Incident ion geometry also affects ion implantation. Varying surface topography across a sample causes the ion incidence angle to deviate from normal (0°), resulting in shallower ion penetration depths (e.g., Liu et al., 2020). However, our TEM analyses show thicker (not thinner) ion-affected regions than predicted by SRIM, and thus invalidate the variation in incidence angle explanation. In contrast, vesiculation likely contributes to the thicker ion-affected regions observed in our experimentally space-weathered samples. The formation of vesicles during ion irradiation decreases the average density of the substrate, allowing ions to penetrate farther into the sample and cause structural disorder up to a greater depth. The timing of vesicle formation—whether they form early, middle, or late during experimental irradiation—also plays an important role in the depth of ion-processed zones, with earlier formation leading to increased thickness. In this context, the He<sup>+</sup>-irradiated Fe-rich olivine sample (Fig. 10) is of particular interest. This sample's ion-affected region, which is significantly more vesiculated than the He<sup>+</sup>-irradiated Mg-rich olivine, exceeds the estimated SRIM thickness by ~70–150%, while the thickness of the He<sup>+</sup>-irradiated Mg-rich olivine sample's ion-affected region is consistent with SRIM estimates. Finally, SRIM calculations do not account for diffusion, changes in substrate chemistry with continued irradiation, progressive amorphization, or ion flux, all of which contribute to ion penetration range and, thus, the thickness of ion-affected zones.

The structural order of ion-affected rims in our samples varies. While complete amorphization is observed in the matrix and He<sup>+</sup>-irradiated Fe-rich olivine cross-sections, the Mg-rich olivine and H<sup>+</sup>-irradiated Fe-rich olivine cross-sections show evidence of nanocrystallinity. These nanocrystalline regions likely represent recrystallization in areas where the crystal structure had sufficient time (on the order of picoseconds) to regain short-range order following collisions with incident ions. This result may suggest that similar partially amorphous space-weathered rims can be expected in returned samples from asteroids Bennu and Ryugu.

Experiments using 4 keV He<sup>+</sup> performed by Carrez et al. (2002) and Christoffersen et al. (2020) suggested that complete amorphization of Mg-rich olivine occurs at a fluence between  $1 \times 10^{16}$  and  $5 \times 10^{16}$  He<sup>+</sup>/cm<sup>2</sup>. Comparatively, this study's He<sup>+</sup>-irradiated olivine samples experienced a total fluence that was two orders of magnitude higher than the critical dose ( $1.1 \times 10^{18}$  ions/cm<sup>2</sup>), indicating that the corresponding ion-affected regions should be completely amorphous. Instead, this study's He<sup>+</sup>-irradiated Mg-rich olivine sample is characterized by partial amorphization (Fig. 8). Shadowing—a phenomenon which occurs on rough surfaces and reduces the incident ion fluence—may contribute to this partial amorphization. Alternatively, it may result from differential charging, localized electrostatic fields, or crystal-orientation effects (Li et al., 2013). However, these possibilities are unconfirmed, and the partially amorphous (rather than completely amorphous) nature of our He<sup>+</sup>-irradiated Mg-rich olivine sample remains puzzling.

Unlike the He<sup>+</sup>-irradiated olivine samples, both H<sup>+</sup>-irradiated olivine cross-sections contain nanocrystalline regions (Figs. 9 and 11). Reduction of the effective fluence received by local areas of the sample due to shadowing may have contributed to this nanocrystallinity.

However, it should be noted that the critical amorphization dose of olivine irradiated with 1 keV H<sup>+</sup> is not particularly well-constrained. A recent study by Takigawa et al. (2019) observed vesiculation and partial amorphization of orthoenstatite only after irradiation with 1 keV H<sup>+</sup> up to a dose of  $1 \times 10^{17}$  ions/cm<sup>2</sup>. This may suggest that the experimental fluence employed in our H<sup>+</sup>-irradiation experiments ( $8.1 \times 10^{17}$  H<sup>+</sup>/cm<sup>2</sup>; ~700 yrs. of exposure at Bennu) is too low to cause complete amorphization of olivine in H<sup>+</sup>-irradiated surfaces. More experiments are needed to better understand the crystalline-amorphous transition of olivine irradiated with low energy H<sup>+</sup> ions.

The partially amorphous nature of these three olivine samples (He<sup>+</sup>-irradiated Mg-rich olivine, H<sup>+</sup>-irradiated Mg-rich olivine, and H<sup>+</sup>-irradiated Fe-rich olivine) is also interesting when compared to the microstructure of naturally-irradiated olivine grains from the Moon and Itokawa. Although highly strained, space-weathered rims in the majority of lunar and Itokawa olivine particles, which have experienced comparable or higher ion doses than this study's Murchison sample, are nanocrystalline up to the surface and contain very few localized regions of amorphous material (Keller and Berger, 2014; Noguchi et al., 2011, 2014b; Thompson et al., 2014). Overall, our olivine samples exhibit greater amorphization than these returned samples. Additionally, unlike lunar and Itokawa olivine grains, other mineral phases returned from the same parent bodies (e.g., plagioclase and pyroxene) contain completely amorphous zones at or near their surfaces (e.g., Keller et al., 2016; Keller and Berger, 2014; Noguchi et al., 2014b; Thompson et al., 2014). According to laboratory ion irradiation experiments, as discussed above, olivine grains are predicted to exhibit completely amorphous zones, considering the surface exposure times predicted for the Moon and asteroid Itokawa from solar flare track and isotopic measurements (e.g., Christoffersen et al., 2020; Keller et al., 2016). One possible explanation for the crystallinity discrepancy between experimentally- and naturally-irradiated olivine is a flux effect, because laboratory experiments employ ion fluxes ~5–6 orders of magnitude higher than actual solar wind (Christoffersen et al., 2020). This highlights the need for low flux H<sup>+</sup> and He<sup>+</sup> ion irradiation experiments to unravel the paradox of solar wind microstructural damage in olivine grains.

#### 4.2.2. Vesiculation

Vesicles form when the concentration of implanted H and He exceeds what the crystal structure can accommodate in the form of isolated point defects, and the implanted species begin to congregate to form voids (i.e., “bubbles”). Although vesicles are considered a characteristic feature of experimentally ion irradiated and laser irradiated mineral and meteorite samples, including anhydrous silicates, some sulfides and oxides, and carbonaceous chondrites (e.g., Carrez et al., 2002; Chaves et al., 2020; Christoffersen et al., 2010; Demyk et al., 2001; Gillis-Davis et al., 2017; Keller et al., 2015a; Matsuoka et al., 2015, 2020; Thompson et al., 2019, 2020), the conditions required for their formation and preservation in returned samples and their impact on the development of ion-processed zones are not well constrained (Assonov et al., 1998; Brownlee et al., 1998; Keller and McKay, 1997; Matsumoto et al., 2014, 2015; Noble et al., 2005; Noguchi et al., 2014b; Phakey et al., 1972; Thompson et al., 2014).

Vesicles are relatively uncommon in space-weathered rims of lunar soils, but, when present, they are roughly 20–80 nm in size (e.g., Keller and McKay, 1993, 1997). In contrast, silicate Itokawa grains contain lenticular vesicles approximately 50–60 nm in length and 15–20 nm in height, which tend to occur within the outermost ~50 nm of grain surfaces rather than throughout the full width of space-weathered rims (Matsumoto et al., 2014, 2015; Noguchi et al., 2014b; Thompson et al., 2014). More recently, vesicles were identified in space-weathered rims of sulfide Itokawa particles (Matsumoto et al., 2020; Matsumoto et al., 2021). Vesiculation density in Itokawa samples varies from grain to grain, and some silicate particles exhibit potential precursor or collapsed vesicles at greater depths (Matsumoto et al., 2014, 2015; Noguchi et al., 2014b; Thompson et al., 2014). Lunar sample analyses have suggested

that vesiculation requires both localized heating from an impact event as well as implantation of solar wind H and He ions (Brownlee et al., 1998; Keller and McKay, 1997; Noble et al., 2005; Thompson et al., 2014, 2017), whereas vesiculated rims in Itokawa grains are predominantly attributed to solar wind irradiation, specifically by He ions (Matsumoto et al., 2014, 2015; Noguchi et al., 2014b; Thompson et al., 2014). The presence of vesicles throughout the ion-processed regions of all samples analyzed in this study suggests that both H and He ion implantation can form vesicles and demonstrates the importance of ion flux in this process. Natural solar wind has a flux of  $10^8$  ions/cm<sup>2</sup>/s at 1 AU while ion irradiation experiments, like those performed here, use fluxes ~4–5 orders of magnitude higher (e.g., Christoffersen et al., 2020; Dukes et al., 1999; Loeffler et al., 2009; Takigawa et al., 2019). The higher flux employed in our experiments likely affects the size, shape, density, and lifespan of vesicles in our experimentally space-weathered samples. More specifically, higher irradiation fluxes may limit the ability of solid-state diffusion to prevent the saturation of implanted ions and formation of implantation bubbles. Therefore, for the same ion fluence, the high-flux experimental conditions could be expected to favor bubble formation, compared to the lower solar wind flux experienced by natural samples.

The H<sup>+</sup>- and He<sup>+</sup>-irradiated matrix cross-sections (Figs. 6 and 7) and He<sup>+</sup>-irradiated Fe-rich olivine cross-section (Fig. 10) exhibit the greatest vesiculation, and the He<sup>+</sup>-irradiated Fe-rich olivine sample is significantly more vesiculated than other irradiated olivine cross-sections from this study (Fig. 10). Secondary electron images show that this intense vesiculation in the He<sup>+</sup>-irradiated Fe-rich olivine sample is evident as blistering on the sample's surface (Fig. 10C). Such blistering was also observed in Fe-Mg-silicate grains in Itokawa dust particles (Matsumoto et al., 2014, 2015; Noguchi et al., 2014b). Differences in the extent of olivine vesiculation in this study may result from effects associated with shadowing, crystal orientation, local surface topography, and/or varying substrate Mg/Fe ratios (e.g., Li et al., 2013; Wang and Ewing, 1992; Wang et al., 1993).

#### 4.3. Chemical changes

In addition to microstructural modifications (e.g., amorphization and vesiculation), ion irradiation processes also result in distinct compositional changes in minerals. Three samples analyzed in this study (He<sup>+</sup>-irradiated Mg-rich olivine, H<sup>+</sup>-irradiated Mg-rich olivine, and H<sup>+</sup>-irradiated Fe-rich olivine) (Figs. 8, 9, and 11) exhibit chemical heterogeneity in their ion-processed regions, although their chemical characteristics are heterogeneous across mineral phase and even within the same sample. One notable trend observed in these samples is the presence of an amorphous, Si-enriched, Mg-Fe-depleted layer at or near the sample's surface. This layer varies laterally across the cross-sections in its distribution, its thickness, and in its chemical concentration of Si. Other studies have identified Si-rich layers within the space-weathered rims of Itokawa and lunar regolith grains (Burgess and Stroud, 2018a, 2018b; Keller and Berger, 2014; Matsumoto et al., 2020; Noguchi et al., 2014a, 2014b). Interestingly, in the case of our H<sup>+</sup>-irradiated Fe-rich olivine sample, the Si-enriched, Mg-Fe-depleted layer is overlain by a thin (2–5 nm) region that is enriched in Mg and Fe and depleted in Si. A similar chemical variation with depth was observed in some Itokawa olivine and orthopyroxene grains (Noguchi et al., 2014a, 2014b; Thompson et al., 2014). Recoil mixing, preferential sputtering, redeposition of sputtered material, and recondensation of melt/vapor derived from micrometeoroid impacts have all been proposed as possible origins of chemically distinct layers seen in previous space weathering studies.

The chemical changes in our samples are complex and difficult to explain with any single ion processing mechanism. Other investigations of experimentally space-weathered samples and returned samples have also identified signatures indicative of multifaceted ion interactions (e.g., Christoffersen et al., 1996; Matsumoto et al., 2020; Noguchi et al.,

2014a, 2014b; Thompson et al., 2014). Here, we discuss a few processes that likely work in concert to form the compositional effects described above. It is also important to note that exposure to the ambient atmosphere between performing different analytical techniques could affect surface chemistry. More specifically, Cantando et al. (2008) showed that surface Mg content in ion irradiated samples will deplete due to cation exchange with adsorbed H<sub>2</sub>O (Cantando et al., 2008). Additional studies comparing chemical results from ion irradiation experiments to models of ion-surface interactions are needed in order to better determine the mechanisms that may be driving changes in surface chemistry in naturally space-weathered samples.

Sputtering is a surface phenomenon (1–5 nm deep) in which collisions between incident ions and target atoms result in the removal of substrate target atoms. The efficiency of sputtering is influenced by incidence angle, with oblique incidence sputtering at a greater rate than normal incidence (Johnson, 1989; Wehner, 1959). Most multicomponent materials do not sputter stoichiometrically; the preference by which target atoms are removed is predominantly determined by their mass but also by surface binding energy and target composition (i.e., target elemental abundances). This process of preferential sputtering has been commonly invoked to explain surface layers that exhibit non-stoichiometric concentrations of elements indigenous to the unaltered substrate in both experimentally-irradiated materials and natural lunar and Itokawa samples (e.g., Carrez et al., 2002; Dukes et al., 1999; Keller and McKay, 1997; Noguchi et al., 2014b). In our olivine samples, O and Mg (the lighter atoms), may be preferentially sputtered, leaving behind an enrichment in Si. Such Mg and O depletions were observed in previous low energy H<sup>+</sup>- and He<sup>+</sup>-irradiation experiments of olivine (e.g., Bradley et al., 1996; Carrez et al., 2002; Demyk et al., 2001). However, surface chemical heterogeneity in our samples extends to depths greater than can be accounted for by preferential sputtering alone (i.e., >~10 nm). Experimental and theoretical investigations have shown that sputter re-deposition is more effective on rough surfaces, like powdered samples, than flat surfaces, with ~66–90% of sputtered material being re-deposited on ion irradiated powdered samples (e.g., Cassidy and Johnson, 2005; Hapke and Cassidy, 1978; Loeffler et al., 2009). We note that the extent to which sputter re-deposition may be occurring in our experiments is uncertain, for the surface roughness of our Murchison sample likely falls between that of a polished, flat surface and a typical powdered sample and exhibits lateral heterogeneity (i.e., surface roughness differs between matrix regions and chondrules).

A second mechanism—recoil implantation—alters surface chemistry, non-thermally, through knock-on collisions that displace target atoms deeper into the substrate material (Kelly and Sanders, 1976; Sigmund, 1979, 1981). In multicomponent materials, lighter elements (like Mg and O) are displaced deeper into the sample than their heavier counterparts (like Si). Prior to achieving steady-state concentrations, the lighter elements concentrate at depth within the sample while heavier elements concentrate near the surface. Christoffersen et al. (1996) proposed this a possible mechanism for widening of Fe-poor radiation-damaged layers in lunar ilmenite grains, although experiments have shown that this process can only increase layer thicknesses by tens of nanometers (Kelly and Sanders, 1976).

Another mechanism that may be contributing to chemical trends in our samples is radiation-enhanced diffusion (RED). This mechanism is driven by compositional gradients created by preferential sputtering and/or recoil implantation. This gradient causes mobile atoms from deeper within the irradiated region of the sample to diffuse toward the surface in attempt to reach equilibrium. In this way, RED can increase the thicknesses of chemically distinct layers and, thus, may be particularly applicable to the Si-enriched, Mg-depleted layers in our samples that are wider than what is expected from preferential sputtering alone. This effect has been observed in many binary alloys subjected to ion irradiation (Ho, 1978) and was proposed as a possible explanation for chemical trends in lunar ilmenite grain surfaces (Christoffersen et al., 1996). The effectiveness of this diffusion process depends on the amount

of crystallographic damage in the ion-affected region, the relative mobility of the constituent atoms, and the temperature of the environment (Cheng et al., 1992 and references therein; Ho, 1978; Sigmund, 1981). In all likelihood, the chemical signatures observed in our EDX analyses result from complex and simultaneous interactions among sputtering, segregation, and diffusion mechanisms induced by ion irradiation.

#### 4.4. Volatiles

Carbonaceous chondrites contain ~2–4 wt% carbon, the majority of which (~70–90%) exists as complex, insoluble, kerogen-like macromolecules called insoluble organic matter (IOM) (e.g., Gardiner et al., 2000; Murae et al., 1990; Pearson et al., 2006; Pizzarello et al., 2006; Sephton, 2002). Our XPS analyses, which probe the outermost ~10 nm of our sample, show that both H<sup>+</sup>- and He<sup>+</sup>-irradiation remove significant amounts of surface carbon, including any that is adventitious (i.e., contaminant sourced from the ambient atmosphere) (Figs. 2 and 3). The  $\mu$ L<sup>2</sup>MS analyses (Fig. 5), which detect nearly all desorbable free organic species, indicate that organic components react differently to He<sup>+</sup>- and H<sup>+</sup>-irradiation. He<sup>+</sup>-irradiation decreases bulk organic content while H<sup>+</sup>-irradiation slightly increases the concentration of some low-molecular-weight free organic species, likely without changing bulk organic abundance. Previous investigations have shown that organic matter within Murchison's matrix material is heterogeneous in its distribution, composition, and structure (e.g., Pizzarello et al., 2006; Sephton, 2002), which may complicate some of this study's interpretations.

The relative efficiencies of H<sup>+</sup> and He<sup>+</sup> at altering organics in Murchison may be related to ion composition, scattering cross-section, and kinetic energy. Four keV He<sup>+</sup> ions, which penetrate deeper into the sample and deposit more energy, are more efficient at fragmenting and breaking bonds in organic matter compared to H<sup>+</sup> ions, which have a lower energy and are implanted at shallower depths. Our results indicate that He<sup>+</sup>-irradiation breaks carbon bonds in organic matter, including both the volumetrically dominant IOM as well as free organics, and sputters the constituent atoms and molecules. Alternatively, H<sup>+</sup>-irradiation appears to increase the abundance of some low-molecular-weight free species by fragmenting macromolecular IOM, which cannot be detected by the  $\mu$ L<sup>2</sup>MS instrument, into smaller organic components which can be detected by  $\mu$ L<sup>2</sup>MS. Thus, H<sup>+</sup>-irradiation is not increasing the bulk organic content but rather increasing the amount of detectable free organic species in Murchison's matrix through fragmentation of IOM. Another possibility is that H<sup>+</sup>-irradiation synthesizes new organic species. For example, proton irradiation experiments performed on powdered graphite by Starukhina et al. (1990) lead to the formation of PAHs. Additional experiments are needed to better understand this mechanism of organic synthesis.

The reduction in organic species observed in the He<sup>+</sup>-irradiated area contrasts with results from our H<sup>+</sup>-irradiation experiment and previous experiments simulating space weathering processes on Murchison, namely micrometeoroid bombardment. Similar to our H<sup>+</sup>-irradiation experiment, progressive laser irradiation of the Murchison meteorite increased the abundance of polycyclic aromatic hydrocarbons by breaking down macromolecular IOM (Thompson et al., 2020). These results may be significant, as they indicate that solar wind He<sup>+</sup>-irradiation, solar wind H<sup>+</sup>-irradiation, and micrometeoroid bombardment change the functional group chemistry of organic carbon on airless body surfaces in different ways. Additionally, ion irradiation of natural complex hydrocarbons (e.g., asphalitite and kerite), which are analogs for IOM on primitive asteroids, cause bluing of VNIR spectral slopes (Moroz et al., 2004) while our experiments show spectral reddening. These opposing spectral trends may result from the use of isolated organic phases in Moroz et al. (2004) rather than a multi-phase material dominated by silicate minerals, which are known to redden with exposure to ion bombardment, like the Murchison sample used in this study.

(e.g., Loeffler et al., 2009). Together, these findings suggest that organic material and silicate phases respond differently to irradiation by solar wind H<sup>+</sup> and He<sup>+</sup> ions and that constituent space weathering processes (i.e., solar wind vs. micrometeoroid bombardment) may be affecting the concentration of organics in conflicting ways. These conflicting responses may contribute to the variable aliphatic organic mixture signatures recently identified on asteroid Bennu with the OSIRIS-REx Visible and InfraRed Spectrometer (OVIRS; 0.4–4.3 μm) (Kaplan et al., 2020).

In addition to examining changes in organic abundances and chemistries, μL<sup>2</sup>MS analyses also suggest that H<sub>2</sub>O abundance increases with H<sup>+</sup>- and He<sup>+</sup>-irradiation (~66% and ~33% increase, respectively) (Fig. 5). A small increase in OH<sup>-</sup> abundance is also observed in ion irradiated spectra. The differences in OH<sup>-</sup>/H<sub>2</sub>O content in the unirradiated, H<sup>+</sup>-irradiated, and He<sup>+</sup>-irradiated Murchison surfaces may be explained by decomposition of matrix phyllosilicates, sample heterogeneity, in situ production of water by radiolysis and H<sup>+</sup>-implantation, or a combination of some, or all, of these mechanisms. It is important to note that VNIR spectra show only minor changes in the absorption strengths of OH<sup>-</sup> and H<sub>2</sub>O bands as a result of ion irradiation (Fig. 4). Considering these spectra were acquired under ambient laboratory conditions, variations between the unirradiated, H<sup>+</sup>-irradiated, and He<sup>+</sup>-irradiated spectra are likely an artifact of terrestrial water adsorption. Differences in the sensitivity and information depth of these analytical techniques likely also contribute to these contradictory results (μL<sup>2</sup>MS is much more surface sensitive than VNIR, Fig. 1B). Below, we present possible explanations for the increased H<sub>2</sub>O content indicated by μL<sup>2</sup>MS.

Ion irradiation has been shown to cause structural breakdown of matrix phyllosilicate minerals and subsequent release of OH<sup>-</sup> and H<sub>2</sub>O from their crystal structure (Keller et al., 2015a, 2015b, 2015c; Thompson et al., 2019, 2020). The liberated hydroxyl and water may reside in vesicles within space-weathered surface layers where it can be easily volatilized by the μL<sup>2</sup>MS infrared laser. If the structural breakdown of matrix phyllosilicate minerals was the sole reason for the increased OH<sup>-</sup>/H<sub>2</sub>O abundance observed in this study, He<sup>+</sup>-irradiation should result in greater OH<sup>-</sup>/H<sub>2</sub>O content due to its greater penetration depth compared to H<sup>+</sup>. The higher H<sub>2</sub>O content observed in the H<sup>+</sup>-irradiated region suggests that the decomposition of phyllosilicates is not the only mechanism contributing to increased water content.

In the case of the H<sup>+</sup>-irradiated surface, a possible explanation for the increased water content is in situ formation. Bonds involving the cations Mg and Si in various silicate minerals can be broken by ion irradiation-induced sputtering, leaving behind a stoichiometric excess of reactive free O or OH<sup>-</sup>. When H<sup>+</sup> ions are implanted into the surface of the grain, H<sub>2</sub>O and OH<sup>-</sup> bonds can form (Bradley et al., 2014; Ichimura et al., 2012; Schaible and Baragiola, 2014). Recently, Nakauchi et al. (2021) showed that H<sup>+</sup>-irradiation can produce H<sub>2</sub>O and Si-OH in both hydrous and anhydrous mineral phases by breaking Si-O-Si bonding in tetrahedra. These processes may contribute to the higher H<sub>2</sub>O abundance observed in this study's H<sup>+</sup>-irradiated spectrum compared to the He<sup>+</sup>-irradiated spectrum.

Varying proportions of phyllosilicate phases (e.g., serpentines) within the areas analyzed by μL<sup>2</sup>MS and VNIR also could contribute to differences in OH<sup>-</sup>/H<sub>2</sub>O content in the unirradiated, H<sup>+</sup>-irradiated, and He<sup>+</sup>-irradiated surfaces. Additionally, it is possible that μL<sup>2</sup>MS analyses are partially detecting adsorbed water on the surface of the sample sourced from atmospheric interaction rather than intrinsic unbound water or OH<sup>-</sup>/H<sub>2</sub>O in phyllosilicates. By breaking surface bonds, ion irradiation may be creating more sites at which adsorbed water can attach. Regardless, μL<sup>2</sup>MS results may suggest that solar wind irradiation can produce unbound water on the surfaces of airless bodies like Bennu and Ryugu, affecting the overall surface composition of these target asteroids.

Overall, this study shows that space weathering of primitive, carbon-rich regolith by solar wind irradiation and micrometeoroid

bombardment is complex, and the chemical and/or physical changes induced by each space weathering process may generate opposing spectral trends. Analyses carried out, thus far, using remote sensing data from asteroids Bennu and Ryugu further support this complexity, and, similar to previous experimental investigations (e.g., Lantz et al., 2015, 2017), suggest that the surface evolution of carbonaceous asteroids depends on original composition (e.g., initial albedo, hydration, carbon content, etc.) (DellaGiustina et al., 2020). Additional experimental studies, such as this one, that investigate the spectral, chemical, and microstructural effects of space weathering through coordinated analyses on a variety of carbonaceous chondrites subjected to a range of space weathering conditions are necessary to accurately analyze orbital data and returned samples from missions visiting carbon-rich small bodies.

## 5. Conclusion

In this study, we irradiated a small slab of the Murchison CM2 meteorite with 4 keV He<sup>+</sup> and 1 keV H<sup>+</sup> ions to simulate solar wind irradiation of carbonaceous asteroids. We analyzed the spectral, microstructural, and chemical changes of both inorganic and organic phases to investigate the surface evolution of near-Earth and main belt asteroids. We observed significant decreases in surficial carbon content, minor chemical reduction of surface Fe<sup>3+</sup> and Fe<sup>2+</sup>, spectral reddening and brightening in He<sup>+</sup>-irradiated Murchison, and mild spectral reddening in H<sup>+</sup>-irradiated Murchison. The reddening trend likely reflects the decomposition of phyllosilicates (and a small amount of olivine) and subsequent formation of reduced Fe-bearing amorphous material. Minor production of npFe<sup>0</sup> may also contribute to reddening, specifically for the He<sup>+</sup>-irradiated region. Spectral brightening caused by He<sup>+</sup>-irradiation may result from surface roughening, differences in the abundance of chondrules in each analyzed region, the chemical reduction of Fe, and/or the removal of surface carbon. The effect of ion irradiation on volatile species is complex. Regarding the distribution of organic carbon, He<sup>+</sup>-irradiation decreases bulk organic content while H<sup>+</sup>-irradiation fragments organic macromolecules, resulting in a relative increase in some low-molecular-weight free organic species. Additionally, μL<sup>2</sup>MS analysis suggests that H<sup>+</sup>- and He<sup>+</sup>-irradiation may increase the abundance of OH<sup>-</sup>/H<sub>2</sub>O within the irradiated regions through a combination of phyllosilicate decomposition, in situ water formation, and/or adsorption of OH<sup>-</sup>/H<sub>2</sub>O from the ambient atmosphere. Microstructural analysis showed complete amorphization of phyllosilicate minerals in the ion-affected regions of matrix cross-sections and partial amorphization of olivine cross-sections. We identified nanoparticles in the He<sup>+</sup>-irradiated matrix cross-section only. Both H<sup>+</sup>- and He<sup>+</sup>-irradiation yield ion-processed surfaces that are thicker than estimates from SRIM calculations, likely resulting from high ion fluxes, decreased substrate density from vesiculation, and other factors not modeled by the SRIM software. Also, we observed changes in Si and Mg abundances at the surfaces of olivine cross-sections that cannot be easily attributed to a single mechanism. Rather, this chemical heterogeneity may form through a combination of sputtering, segregation, and diffusion processes. Results from this study highlight the complex nature and often conflicting effects of space weathering of carbonaceous materials including a heterogeneous distribution of silicate and organic phases.

While laboratory space weathering experiments cannot perfectly replicate natural space weathering processes, they do provide valuable insight into the spectral, microstructural, and chemical effects that may be observed in samples returned from carbonaceous asteroids. Based on findings from this study and others, we hypothesize that returned regolith samples from Bennu and Ryugu will be characterized by completely amorphous phyllosilicate rims with greater vesiculation than has been previously observed in returned samples from the Moon and Itokawa and partially amorphous olivine rims with Si-enriched surface layers. While vesiculation in returned olivine grains from Bennu and

Ryugu will likely not be as extensive as this study's experimentally-irradiated samples, some vesiculation is expected from solar wind ion implantation, similar to blistering seen on the surfaces of Itokawa grains. Chemically, our results are variable and complex, making it difficult to predict the compositional characteristics of space-weathered rims in natural samples. Having been exposed to both solar wind irradiation and micrometeoroid bombardment, nanophase Fe and Fe-sulfides will likely be present, similar to Itokawa particles (Keller and Berger, 2014; Noguchi et al., 2011, 2014a, 2014b; Thompson et al., 2014), and possibly nanophase Fe-Ni-sulfides and magnetite, which were identified in laser irradiated Murchison samples (Thompson et al., 2019, 2020). The analysis of returned samples from asteroids Bennu and Ryugu will provide ground-truth for our experiments and improve our understanding of space weathering as it operates across the solar system.

### Declaration of Competing Interest

The authors declare that they have no known competing financial interests or personal relationships that could have appeared to influence the work reported in this paper.

### Acknowledgments

This research was supported by NASA Solar System Workings grant 80NSSC19K0960. Utilization of the University of Virginia's NMCF Versaprobe III XPS was fundamental to this project, and, therefore, we acknowledge NSF MRI award #1626201 for the acquisition of this instrument. We also acknowledge the use of Electron Beam Analysis Labs at the NASA Johnson Space Center and greatly thank Zia Rahman for his help in preparing focused ion beam cross-sections for TEM analysis. We gratefully recognize the Center for Meteorite Studies at Arizona State University for providing the Murchison sample (catalog # 828) used in these experiments. Finally, we sincerely thank our reviewers, Moe Matsuoka and Rosario Brunetto, for their constructive and insightful feedback which greatly improved this manuscript.

### References

- Abe, M., Takagi, Y., Kitazato, K., Abe, S., Hiroi, T., Vilas, F., Clark, B.E., Abell, P.A., Lederer, S.M., Jarvis, K.S., Nimura, T., Ueda, Y., Fujiwara, A., 2006. Near-infrared spectral results of asteroid Itokawa from the Hayabusa spacecraft. *Science* 312, 1334–1338.
- Adams, J.B., McCord, T.B., 1971a. Alteration of lunar optical properties: age and composition effects. *Science* 171, 567–571.
- Adams, J.B., McCord, T.B., 1971b. Optical properties of mineral separates, glass, and anorthositic fragments from Apollo mare samples. In: Proceedings of the 2<sup>nd</sup> Lunar Science Conference, pp. 2183–2195.
- Adams, J.B., McCord, T.B., 1973. Vitrification darkening of lunar highlands and identification of Descartes material at the Apollo 16 site. In: Proceedings of the 4<sup>th</sup> Lunar Science Conference, pp. 163–177.
- Allen, C.C., Morris, R.V., Lauer Jr., H.V., McKay, D.S., 1993. Effects of microscopic iron metal on the reflectance spectra of glass and minerals. In: 24<sup>th</sup> Lunar and Planetary Science Conference, pp. 17–18.
- Assonov, S.S., Biryukov, A.Y., Kashkarov, L.L., Nevezorov, V.N., Semenova, A.S., Shukolyukov, Y.A., 1998. Vesiculation in silicate grains of Luna-16 soil. In: 29<sup>th</sup> Lunar and Planetary Science Conference (Abstract # 1635).
- Barr, T.L., Seal, S., 1995. Nature of the use of adventitious carbon as a binding energy standard. *J. Vac. Sci. Technol. A* 13, 1239–1246.
- Beck, P., Quirico, E., Montes-Hernandez, G., Bonal, L., Bolland, J., Orthous-Daunay, F.-R., Howard, K., Schmitt, B., Brissaud, O., 2010. Hydrous mineralogy of CM and CI chondrites from infrared spectroscopy and their relationship with low albedo asteroids. In: 41<sup>st</sup> Lunar and Planetary Science Conference (Abstract # 1586).
- Biesinger, M.C., Payne, B.P., Grosvenor, A.P., Lau, L.W.M., Gerson, A.R., Smart, R.S.C., 2011. Resolving surface chemical states in XPS analysis of first row transition metals, oxides and hydroxides: Cr, Mn, Fe, Co and Ni. *Appl. Surf. Sci.* 257, 2717–2730.
- Bishop, J.L., Michalski, J.R., Carter, J., 2017. Remote Detection of Clay Minerals. In: Gates, W.P., Kloprogge, J.T., Madejová, J., Bergaya, F. (Eds.), *Infrared and Raman Spectroscopies of Clay Minerals*, 8. Elsevier, pp. 482–514.
- Blanco, A., Bussolotti, E., Colangeli, L., 1988. A mixture of hydrogenated amorphous carbon grains and PAH molecules: a candidate for the unidentified infrared bands? *Astrophys. J.* 334, 875–882.
- Bland, P.A., Cresssey, G., Menzies, O.N., 2004. Modal mineralogy of carbonaceous chondrites by X-ray diffraction and Mössbauer spectroscopy. *Meteorit. Planet. Sci.* 39, 3–16.
- Bland, P.A., Zolensky, M.E., Benedix, G.K., Sephton, M.A., 2006. Weathering of chondritic meteorites. In: Lauretta, D.S., McSween, H.Y. (Eds.), *Meteorites and the Early Solar System II*. University of Arizona Press, Tucson, pp. 853–867.
- Bradley, J.P., Dukes, C., Baragiola, R., McFadden, L., Johnson, R.E., Brownlee, D.E., 1996. Radiation processing and the origins of interplanetary dust. In: 27<sup>th</sup> Lunar and Planetary Science Conference, pp. 149–150.
- Bradley, J.P., Ishii, H.A., Gillis-Davis, J.J., Ciston, J., Nielsen, M.H., Bechtel, H.A., Martin, M.C., 2014. Detection of solar wind-produced water in irradiated rims on silicate minerals. *Proc. Natl. Acad. Sci. U. S. A.* 111, 1732–1735.
- Britt, D.T., Tholen, D.J., Bell, J.F., Pieters, C.M., 1992. Comparison of asteroid and meteorite spectra: classification by principal component analysis. *Icarus* 99, 153–166.
- Brownlee, D.E., Joswiak, D.J., Bradley, J.P., Schlutter, D.J., Pepin, R.O., 1998. Tiny bubbles: direct observation of He in IDPs. In: 29<sup>th</sup> Lunar and Planetary Science Conference (Abstract # 1869).
- Brunetto, R., Lantz, C., Ledu, D., Baklouti, D., Barucci, M.A., Beck, P., Delauche, L., Dionnet, Z., Dumas, P., Duprat, J., Engrand, C., Jamme, F., Oudayer, P., Quirico, E., Sandt, C., Dartois, E., 2014. Ion irradiation of Allende meteorite probed by visible, IR, and Raman spectroscopies. *Icarus* 237, 278–292.
- Brunetto, R., Strazzulla, G., 2005. Elastic collisions in ion irradiation experiments: a mechanism for space weathering of silicates. *Icarus* 179, 265–273.
- Burgess, K.D., Stroud, R.M., 2018a. Phase-dependent space weathering effects and spectroscopic identification of retained helium in a lunar soil grain. *Geochim. Cosmochim. Acta* 224, 64–79.
- Burgess, K.D., Stroud, R.M., 2018b. Coordinated nanoscale compositional and oxidation state measurements of lunar space-weathered material. *J. Geophys. Res. Planets* 123, 2022–2037.
- Burns, R.G., Fisher, D.S., 1994. Nanophase mixed-valence iron minerals in meteorites identified by cryogenic Mössbauer spectroscopy. *Hyperfine Interact.* 91, 571–576.
- Cannon, K.M., Mustard, J.F., Parman, S.W., Sklute, E.C., Dyar, M.D., Cooper, R.F., 2017. Spectral properties of Martian and other planetary glasses and their detection in remotely sensed data. *J. Geophys. Res. Planets* 122, 249–268.
- Cant, J.D.H., Syres, K.L., Lunt, P.J.B., Radtke, H., Treacy, J., Thomas, P.J., Lewis, E.A., Haigh, S.J., Obrien, P., Schulte, K., Bondino, F., Magnano, E., Flavell, W.R., 2015. Surface properties of nanocrystalline PbS films deposited at the water-oil interface: a study of atmospheric aging. *Langmuir* 31, 1445–1453.
- Cantando, E.D., Dukes, C.A., Loeffler, M.J., Baragiola, R.A., 2008. Aqueous depletion of Mg from olivine surfaces enhanced by ion irradiation. *J. Geophys. Res.* 113, E09011.
- Carrez, P., Demyk, K., Cordier, P., Gengembre, L., Grimblot, J., D'Hendecourt, L., Jones, A.P., Leroux, H., 2002. Low-energy helium ion irradiation-induced amorphization and chemical changes in olivine: insights for silicate dust evolution in the interstellar medium. *Meteorit. Planet. Sci.* 37, 1599–1614.
- Carter, A.J., Ramsey, M.S., Durant, A.J., Skilling, I.P., Wolfe, A., 2009. Micron-scale roughness of volcanic surfaces from thermal infrared spectroscopy and scanning electron microscopy. *J. Geophys. Res. Solid Earth* 114, 1–13.
- Cassidy, T.A., Johnson, R.E., 2005. Monte Carlo model of sputtering and other ejection processes within a regolith. *Icarus* 176, 499–507.
- Chaves, L.C., Thompson, M.S., Loeffler, M.J., 2020. Micrometeorite bombardment simulation on Murchison meteorite: the role of sulfides in the space weathering of carbonaceous chondrites. In: 51<sup>st</sup> Lunar and Planetary Science Conference (Abstract # 1670).
- Cheng, Y.-T., Simko, S.J., Militello, M.C., Dow, A.A., Auner, G.W., Alkaissi, M.H., Padmanabhan, K.R., 1992. A comparison between high- and low-energy ion mixing at different temperatures. *Nucl. Inst. Methods Phys. Res. B* 64, 38–47.
- Christoffersen, R., Keller, L.P., McKay, D.S., 1996. Microstructure, chemistry, and origin of grain rims on ilmenite from the lunar soil finest fraction. *Meteorit. Planet. Sci.* 31, 835–848.
- Christoffersen, R., Keller, L.P., Dukes, C., Rahman, Z., Baragiola, R., 2010. Experimental investigation of space radiation processing in lunar soil ilmenite: combining perspectives from surface science and transmission electron microscopy. In: 41<sup>st</sup> Lunar and Planetary Science Conference (Abstract # 1532).
- Christoffersen, R., Keller, L.P., Dukes, C., 2020. The role of solar wind ion processing in space weathering of olivine: Unraveling the paradox of laboratory irradiation results compared to observations of natural samples. In: 51<sup>st</sup> Lunar and Planetary Science Conference (Abstract # 2147).
- Clark, B.E., Hapke, B., Pieters, C., Britt, D., 2002. Asteroid space weathering and regolith evolution. In: Bottke, W.F., Cellino, A., Paolicchi, P., Binzel, R.P. (Eds.), *Asteroids III*. University of Arizona Press, Tucson, pp. 585–599.
- Clark, B.E., Binzel, R.P., Howell, E.S., Cloutis, E.A., Ockert-Bell, M., Christensen, P., Barucci, M.A., DeMeo, F., Lauretta, D.S., Connolly, H., Soderberg, A., Hergenrother, C., Lim, L., Emery, J., Mueller, M., 2011. Asteroid (101955) 1999 RQ36: spectroscopy from 0.4 to 2.4 μm and meteorite analogs. *Icarus* 216, 462–475.
- Clemett, S.J., Zare, R.N., 1997. Microprobe two-step laser mass spectrometry as an analytical tool for meteorite samples. *Int. Astron. Union Symp.* 178, 305–320.
- Clemett, S.J., Messenger, S., Nakamura-Messenger, K., Thomas-Keppta, K.L., McKay, D.S., 2014. Coordinated chemical and isotopic imaging of Bells (CM2) meteorite matrix. In: 45<sup>th</sup> Lunar and Planetary Science Conference (Abstract # 2896).
- Cloutis, E.A., 2015. Fe-bearing glassy materials: spectral reflectance properties. In: 46<sup>th</sup> Lunar and Planetary Science Conference (Abstract # 1234).
- Cloutis, E.A., McCormack, K.A., Bell, J.F., Hendrix, A.R., Bailey, D.T., Craig, M.A., Mertzman, S.A., Robinson, M.S., Riner, M.A., 2008. Ultraviolet spectral reflectance properties of common planetary minerals. *Icarus* 197, 321–347.
- Cloutis, E.A., Hiroi, T., Gaffey, M.J., Alexander, C.M.O., Mann, P., 2011a. Spectral reflectance properties of carbonaceous chondrites: 1. CI chondrites. *Icarus* 212, 180–209.

- Cloutis, E.A., Hudon, P., Hiroi, T., Gaffey, M.J., Mann, P., 2011b. Spectral reflectance properties of carbonaceous chondrites: 2. CM chondrites. *Icarus* 216, 309–346.
- Cloutis, E.A., Hudon, P., Hiroi, T., Gaffey, M.J., 2012. Spectral reflectance properties of carbonaceous chondrites 4: aqueously altered and thermally metamorphosed meteorites. *Icarus* 220, 586–617.
- Court, R.W., Sephton, M.A., 2012. Insights into the nature of cometary organic matter from terrestrial analogues. *Int. J. Astrobiol.* 11, 83–92.
- Court, R.W., Sephton, M.A., Parnell, J., Gilmour, I., 2006. The alteration of organic matter in response to ionising irradiation: chemical trends and implications for extraterrestrial sample analysis. *Geochim. Cosmochim. Acta* 70, 1020–1039.
- Cronin, J.R., Pizzarello, S., Yuen, G.U., 1985. Amino acids of the Murchison meteorite: II. Five carbon acyclic primary  $\beta$ -,  $\gamma$ -, and  $\delta$ -amino alkanoic acids. *Geochim. Cosmochim. Acta* 49, 2259–2265.
- DellaGiustina, D.N., Burke, K.N., Walsh, K.J., Smith, P.H., Golish, D.R., Bierhaus, E.B., Ballouz, L., Becker, T.L., Campins, H., Tatsumi, E., Yumoto, K., Sugita, S., Prasanna Deshapriya, J.D., Cloutis, E.A., Clark, B.E., Hendrix, A.R., Sen, A., Al Asad, M.M., Daly, M.G., Applin, D.M., Aydelliou, C., Barucci, M.A., Becker, K.J., Bennett, C.A., Bottke, W.F., Brodbeck, J.I., Connolly Jr., H.C., Delbo, M., de Leon, J., Drouet d'Aubigny, C.Y., Edmundson, K.L., Fornasier, S., Hamilton, V.E., Hasselmann, P.H., Hergetrother, C.W., Howell, E.S., Jawin, E.R., Kaplan, H.H., Le Corre, L., Lim, L.F., Li, J.-Y., Michel, P., Molaro, J.L., Nolan, M.C., Nolau, J., Pajola, M., Parkinson, A., Popescu, M., Porter, N.A., Rizk, B., Rizos, J.L., Ryan, A.J., Rozitis, B., Shultz, N.K., Simon, A.A., Trang, D., Van Auken, R.B., Wolner, C.W.V., Lauretta, D.S., 2020. Variations in color and reflectance on the surface of asteroid (101955) Bennu. *Science* 370, eabc3660.
- DeMeo, F.E., Alexander, C.M.O'D., Walsh, K.J., Chapman, C.R., Binzel, R.P., 2015. The compositional structure of the asteroid belt. In: Michel, P., DeMeo, F.E., Bottke, W.F. (Eds.), *Asteroids IV*. University of Arizona Press, Tucson, pp. 13–41.
- Demyk, K., Carrez, P., Leroux, H., Cordier, P., Jones, A.P., Borg, J., Quirico, E., Raynal, P. I., D'Hendecourt, L., 2001. Structural and chemical alteration of crystalline olivine under low energy He<sup>+</sup> irradiation. *Astron. Astrophys.* 368, L38–L41.
- Draine, B.T., 1985. Tabulated optical properties of graphite and silicate grains. *Astrophys. J. Suppl. Ser.* 57, 587–594.
- Dukes, C.A., Baragiola, R.A., McFadden, L.A., 1999. Surface modification of olivine by H<sup>+</sup> and He<sup>+</sup> bombardment. *J. Geophys. Res. Planets* 104, 1865–1872.
- Dukes, C.A., Fulvio, D., Baragiola, R.A., 2015. Ion-irradiation induced changes in the surface composition of carbonaceous meteorites. In: *Space Weathering of Airless Bodies: An Integration of Remote Sensing Data, Laboratory Experiments and Sample Analysis Workshop* (Abstract # 2063).
- Gaffey, M.J., Burbine, T.H., Binzel, R.P., 1993. Asteroid spectroscopy: progress and perspectives. *Meteoritics* 28, 161–187.
- Gardinier, A., Derenne, S., Robert, F., Behar, F., Largeau, C., Maquet, J., 2000. Solid state CP/MAS 13C NMR of the insoluble organic matter of the Orgueil and Murchison meteorites: quantitative study. *Earth Planet. Sci. Lett.* 184, 9–21.
- Gillis-Davis, J.J., Lucey, P.G., Bradley, J.P., Ishii, H.A., Connolly, H.C., 2013. Laser space weathering of Allende meteorite. In: *44<sup>th</sup> Lunar and Planetary Science Conference* (Abstract # 2494).
- Gillis-Davis, J.J., Gasda, P.J., Bradley, J.P., Ishii, H.A., Bussey, D.B.J., 2015. Laser space weathering of Allende (CV2) and Murchison (CM2) carbonaceous chondrites. In: *46<sup>th</sup> Lunar and Planetary Science Conference* (Abstract # 1607).
- Gillis-Davis, J.J., Lucey, P.G., Bradley, J.P., Ishii, H.A., Kaluna, H.M., Misra, A., Connolly, H.C., 2017. Incremental laser space weathering of Allende reveals non-lunar like space weathering effects. *Icarus* 286, 1–14.
- Glavin, D.P., Conel, M.O., Aponte, J.C., Dworkin, J.P., Elsila, J.E., Yabuta, H., 2018. The origin and evolution of organic matter in carbonaceous chondrites and links to their parent bodies. In: *Primitive Meteorites and Asteroids: Physical, Chemical, and Spectroscopic Observations Paving the Way to Exploration*. Elsevier, pp. 205–271.
- Glavin, D.P., Elsila, J.E., McLain, H.L., Aponte, J.C., Parker, E.T., Dworkin, J.P., Hill, D. H., Connolly, H.C., Lauretta, D.S., 2020. Extraterrestrial amino acids and L-enantiomeric excesses in the CM2 carbonaceous chondrites Aguas Zarcas and Murchison. *Meteorit. Planet. Sci.* 1–26.
- Glatch, T.D., Bandfield, J.L., Lucey, P.G., Hayne, P.O., Greenhagen, B.T., Arnold, J.A., Ghent, R.R., Paige, D.A., 2015. Formation of lunar swirls by magnetic field standoff of the solar wind. *Nat. Commun.* 6, 6189.
- Gosling, J.T., 2007. The solar wind. In: McFadden, L.A., Weissman, P.R., Johnson, T.V. (Eds.), *Encyclopedia of the Solar System*. Academic Press-Elsevier, Amsterdam, pp. 99–116.
- Hanley, L., Zimmermann, R., 2009. Light and molecular ions: the emergence of vacuum UV single-photon ionization in MS. *Anal. Chem.* 81, 4174–4182.
- Hapke, B., 1973. Darkening of silicate rock powders by solar wind sputtering. *Moon* 7, 342–355.
- Hapke, B., 2001. Space weathering from Mercury to the asteroid belt. *J. Geophys. Res.* 106, 10039–10073.
- Hapke, B., 2008. Bidirectional reflectance spectroscopy. 6. Effects of porosity. *Icarus* 195, 918–926.
- Hapke, B., Cassidy, W., 1978. Is the Moon really as smooth as a billiard ball? Remarks concerning recent models of sputter-fractionation on the lunar surface. *Geophys. Res. Lett.* 5, 5–8.
- Hendrix, A.R., Vilas, F., Li, J.Y., 2016. The UV signature of carbon in the solar system. *Meteorit. Planet. Sci.* 51, 105–115.
- Hiroi, T., Abe, M., Kitazato, K., Abe, S., Clark, B.E., Sasaki, S., Ishiguro, M., Barnouin-Jha, O.S., 2006. Developing space weathering on the asteroid 25143 Itokawa. *Nature* 443, 56–58.
- Hiroi, T., Sasaki, S., Misu, T., Nakamura, T., 2013. Keys to detect space weathering on Vesta: Changes of visible and near-infrared reflectance spectra of HEDs and carbonaceous chondrites. In: *44<sup>th</sup> Lunar and Planetary Science Conference* (Abstract # 1276).
- Ho, P.S., 1978. Effects of enhanced diffusion on preferred sputtering of homogeneous alloy surfaces. *Surf. Sci.* 72, 253–263.
- Hood, L.L., Schubert, G., 1980. Lunar magnetic anomalies and surface optical properties. *Science* 208, 49–51.
- Housley, R.M., Grant, R.W., Paton, N.E., 1973. Origin and characteristics of excess Fe metal in lunar glass welded aggregates. In: *Proceedings of the 4<sup>th</sup> Lunar Science Conference*, pp. 2737–2749.
- Howard, K.T., Benedix, G.K., Bland, P.A., Cressey, G., 2009. Modal mineralogy of CM2 chondrites by X-ray diffraction (PSD-XRD). Part 1: total phyllosilicate abundance and the degree of aqueous alteration. *Geochim. Cosmochim. Acta* 73, 4576–4589.
- Howard, K.T., Benedix, G.K., Bland, P.A., Cressey, G., 2011. Modal mineralogy of CM chondrites by X-ray diffraction (PSD-XRD): part 2. Degree, nature and settings of aqueous alteration. *Geochim. Cosmochim. Acta* 75, 2735–2751.
- Ichimura, A.S., Zent, A.P., Quinn, R.C., Sanchez, M.R., Taylor, L.A., 2012. Hydroxyl (OH) production on airless planetary bodies: evidence from H<sup>+</sup>/D<sup>+</sup> ion-beam experiments. *Earth Planet. Sci. Lett.* 345–348, 90–94.
- Johnson, R.E., 1989. Application of laboratory data to the sputtering. *Icarus* 78, 206–210.
- Johnson, R.E., 1990. *Energetic Charged-Particle Interactions with Atmospheres and Surfaces*. Springer-Verlag Berlin Heidelberg.
- Johnson, T.V., Fanale, F.P., 1973. Optical properties of carbonaceous chondrites and their relationship to asteroids. *J. Geophys. Res.* 78, 8507–8518.
- Kagawa, E., Nakamura, T., Amano, K., Liu, L., Matsuoaka, M., Sasaki, O., 2020. The effects of porosity of surface materials on the reflectance spectra of C-type asteroids PPS07-P11. In: *Japan Geoscience Union - American Geophysical Union Joint Meeting*, pp. PPS07–P11.
- Kaluna, H.M., Ishii, H.A., Bradley, J.P., Gillis-Davis, J.J., Lucey, P.G., 2017. Simulated space weathering of Fe- and Mg-rich aqueously altered minerals using pulsed laser irradiation. *Icarus* 292, 245–258.
- Kaplan, H.H., Lauretta, D.S., Simon, A.A., Hamilton, V.E., DellaGiustina, D.N., Golish, D. R., Reuter, D.C., Bennett, C.A., Burke, K.N., Campins, H., Connolly, H.C., Dworkin, J. P., Emery, J.P., Glavin, D.P., Glatch, T.D., Hanna, R., Ishimaru, K., Jawin, E.R., McCoy, T.J., Porter, N., Sandford, S.A., Ferrone, S., Clark, B.E., Li, J.-Y., Zou, X.-D., Daly, M.G., Barnouin, O.S., Seabrook, J.A., Enos, H.L., 2020. Bright carbonate veins on asteroid (101955) Bennu: implications for aqueous alteration history. *Science* 370, eabc3557.
- Kar, A., Sen, A.K., Gupta, R., 2016. Laboratory photometry of regolith analogues: effect of porosity. *Icarus* 277, 300–310.
- Kar, A., Sen, A.K., Gupta, R., 2021. Laboratory photometry of regolith analogues: effect of porosity-II. *Icarus* 358.
- Keller, L.P., Berger, E.L., 2014. A transmission electron microscope study of Itokawa regolith grains. *Earth, Planets Sp.* 66, 71.
- Keller, L.P., McKay, D.S., 1993. Discovery of vapor deposits in the lunar regolith. *Science* 261, 1305–1307.
- Keller, L.P., McKay, D.S., 1997. The nature and origin of rims on lunar soil grains. *Geochim. Cosmochim. Acta* 61, 2331–2341.
- Keller, L.P., Wentworth, S.J., McKay, D.S., 1998. Space weathering: reflectance spectroscopy and TEM analysis of individual lunar soil grains. In: *29<sup>th</sup> Lunar and Planetary Science Conference* (Abstract # 1762).
- Keller, L.P., Christoffersen, R., Dukes, C.A., Baragiola, R.A., Rahman, Z., 2015a. Ion irradiation experiments on the Murchison CM2 carbonaceous chondrite: simulating space weathering of primitive asteroids. In: *46<sup>th</sup> Lunar and Planetary Science Conference* (Abstract # 1913).
- Keller, L.P., Christoffersen, R., Dukes, C.A., Baragiola, R.A., Rahman, Z., 2015b. Fe and O EELS studies of ion irradiated Murchison CM2 carbonaceous chondrite matrix. In: *78<sup>th</sup> Annual Meeting of the Meteoritical Society* (Abstract # 5354).
- Keller, L.P., Christoffersen, R., Dukes, C.A., Baragiola, R.A., Rahman, Z., 2015c. Experimental space weathering of carbonaceous chondrite matrix. In: *Space Weathering of Airless Bodies: An Integration of Remote Sensing Data, Laboratory Experiments and Sample Analysis Workshop* (Abstract # 2010).
- Keller, L.P., Berger, E.L., Christoffersen, R., Zhang, S., 2016. Direct determination of the space weathering rates in lunar soils and Itokawa regolith from sample analyses. In: *47<sup>th</sup> Lunar and Planetary Science Conference* (Abstract # 2525).
- Kelly, R., Sanders, J.B., 1976. On the role of recoil implantation in altering the stoichiometry of a bombarded solid. *Nucl. Inst. Methods* 132, 335–343.
- Kiuchi, M., Nakamura, A.M., 2014. Relationship between regolith particle size and porosity on small bodies. *Icarus* 239, 291–293.
- Kramer, G.Y., Besse, S., Dhingra, D., Nettles, J., Klima, R., Garrick-Bethell, I., Clark, R.N., Combe, J.P., Head, J.W., Taylor, L.A., Pieters, C.M., Boardman, J., McCord, T.B., 2011. M3 spectral analysis of lunar swirls and the link between optical maturation and surface hydroxyl formation at magnetic anomalies. *J. Geophys. Res.* 116, E00G18.
- Lantz, C., Clark, B.E., Barucci, M.A., Lauretta, D.S., 2013. Evidence for the effects of space weathering spectral signatures on low albedo asteroids. *Astron. Astrophys.* 554, A138.
- Lantz, C., Brunetto, R., Barucci, M.A., Dartois, E., Duprat, J., Engrand, C., Godard, M., Ledu, D., Quirico, E., 2015. Ion irradiation of the Murchison meteorite: visible to mid-infrared spectroscopic results. *Astron. Astrophys.* 577, A41.
- Lantz, C., Brunetto, R., Barucci, M.A., Fornasier, S., Baklouti, D., Bourcqis, J., Godard, M., 2017. Ion irradiation of carbonaceous chondrites: a new view of space weathering on primitive asteroids. *Icarus* 285, 43–57.
- Lauretta, D.S., Bartels, A.E., Barucci, M.A., Bierhaus, E.B., Binzel, R.P., Bottke, W.F., Campins, H., Chesley, S.R., Clark, B.C., Clark, B.E., Cloutis, E.A., Connolly, H.C., Crombie, M.K., Delbo, M., Dworkin, J.P., Emery, J.P., Glavin, D.P., Hamilton, V.E.,

- Hergenrother, C.W., Johnson, C.L., Keller, L.P., Michel, P., Nolan, M.C., Sandford, S.A., Scheeres, D.J., Simon, A.A., Sutter, B.M., Vokrouhlický, D., Walsh, K.J., 2015. The OSIRIS-REx target asteroid (101955) Bennu: constraints on its physical, geological, and dynamical nature from astronomical observations. *Meteorit. Planet. Sci.* 50, 834–849.
- Lauretta, D.S., Balam-Knutson, S.S., Beshore, E., Boynton, W.V., Drouet d'Aubigny, C., DellaGiustina, D.N., Enos, H.L., Golish, D.R., Hergenrother, C.W., Howell, E.S., Bennett, C.A., Morton, E.T., Nolan, M.C., Rizk, B., Roper, H.L., Bartels, A.E., Bos, B.J., Dworkin, J.P., Highsmith, D.E., Lorenz, D.A., Lim, L.F., Mink, R., Moreau, M.C., Nuth, J.A., Reuter, D.C., Simon, A.A., Bierhaus, E.B., Bryan, B.H., Ballouz, R., Barnouin, O.S., Binzel, R.P., Bottke, W.F., Hamilton, V.E., Walsh, K.J., Chesley, S.R., Christensen, P.R., Clark, B.E., Connolly, H.C., Crombie, M.K., Daly, M.G., Emery, J.P., McCoy, T.J., McMahon, J.W., Scheeres, D.J., Messenger, S., Nakamura-Messenger, K., Righter, K., Sandford, S.A., 2017. OSIRIS-REx: sample return from asteroid (101955) Bennu. *Space Sci. Rev.* 212, 925–984.
- Lauretta, D.S., DellaGiustina, D.N., Bennett, C.A., Golish, D.R., Becker, K.J., Balam-Knutson, S.S., Barnouin, O.S., Becker, T.L., Bottke, W.F., Boynton, W.V., Campins, H., Clark, B.E., Connolly, H.C., Drouet d'Aubigny, C.Y., Dworkin, J.P., Emery, J.P., Enos, H.L., Hamilton, V.E., Hergenrother, C.W., Howell, E.S., Izawa, M.R.M., Kaplan, H.H., Nolan, M.C., Rizk, B., Roper, H.L., Scheeres, D.J., Smith, P.H., Walsh, K.J., Wolner, C.W.V., 2019. The unexpected surface of asteroid (101955) Bennu. *Nature* 568, 55–60.
- Lee, S., Keller, L.P., Morris, R.V., Han, J., Rahman, Z., 2020. Thermal decomposition of the Murchison CM2 carbonaceous chondrite: implications of space weathering processes for sample return missions. In: 51<sup>st</sup> Lunar and Planetary Science Conference (Abstract # 2535).
- Li, Y., Li, X., Wang, S., Li, S., Tang, H., Coulson, I.M., 2013. Crystal orientation results in different amorphization of olivine during solar wind implantation. *J. Geophys. Res. E Planet.* 118, 1974–1982.
- Liu, J., Niu, R., Gu, J., Cabral, M., Song, M., Liao, X., 2020. Effect of ion irradiation introduced by focused ion-beam milling on the mechanical behaviour of sub-micron-sized samples. *Sci. Rep.* 10, 1–9.
- Loeffler, M.J., Dukes, C.A., Baragiola, R.A., 2009. Irradiation of olivine by 4 keV He<sup>+</sup>: simulation of space weathering by the solar wind. *J. Geophys. Res.* 114, E03003.
- Lucey, P.G., Noble, S.K., 2008. Experimental test of a radiative transfer model of the optical effects of space weathering. *Icarus* 197, 348–353.
- Lucey, P.G., Riner, M.A., 2011. The optical effects of small iron particles that darken but do not reddens: evidence of intense space weathering on Mercury. *Icarus* 212, 451–462.
- Matsumoto, T., Noguchi, T., Tobimatsu, Y., Harries, D., Langenhorst, F., Miyake, A., Hidaka, H., 2021. Space weathering of iron sulfides in the lunar surface environment. *Geochimica et Cosmochimica Acta* 299, 69–84.
- Matsumoto, T., Tsuchiyama, A., Miyake, A., Noguchi, T., Nakamura, T., Nakamura, M., Matsuno, J., Shimada, A., Uesugi, K., Nakano, T., 2014. Surface micromorphologies of regolith particles from asteroid Itokawa and its implication to space weathering. In: 77<sup>th</sup> Annual Meteoritical Society Meeting (Abstract # 5130).
- Matsumoto, T., Tsuchiyama, A., Miyake, A., Noguchi, T., Nakamura, M., Uesugi, K., Takeuchi, A., Suzuki, Y., Nakano, T., 2015. Surface and internal structures of a space-weathered rim of an Itokawa regolith particle. *Icarus* 257, 230–238.
- Matsumoto, T., Harries, D., Langenhorst, F., Miyake, A., Noguchi, T., 2020. Iron whiskers on asteroid Itokawa indicate sulfide destruction by space weathering. *Nat. Commun.* 11, 1–8.
- Matsuoka, M., Nakamura, T., Kimura, Y., Hiroi, T., Nakamura, R., Okumura, S., Sasaki, S., 2015. Pulse-laser irradiation experiments of Murchison CM2 chondrite for reproducing space weathering on C-type asteroids. *Icarus* 254, 135–143.
- Matsuoka, M., Nakamura, T., Hiroi, T., Okumura, S., Sasaki, S., 2020. Space weathering simulation with low-energy laser irradiation of Murchison CM chondrite for reproducing micrometeoroid bombardments on C-type asteroids. *Astrophys. J.* 890, L23.
- Morota, T., Sugita, S., Cho, Y., Kanamaru, M., Tatsumi, E., Sakatani, N., Honda, R., Hirata, N., Kikuchi, H., Yamada, M., Yokota, Y., Kameda, S., Matsuoka, M., Sawada, H., Honda, C., Kouyama, T., Ogawa, K., Suzuki, H., Yoshioka, K., Hayakawa, M., Hirata, N., Hirabayashi, M., Miyamoto, H., Michikami, T., Hiroi, T., Hemmi, R., Barnouin, O.S., Ernst, C.M., Kitazato, K., Nakamura, T., Liu, L., Senshu, H., Kobayashi, H., Sasaki, S., Komatsu, G., Tanabe, N., Fujii, Y., Irie, T., Suemitsu, M., Takaki, N., Sugimoto, C., Yamamoto, H., Matsuoka, M., Kato, H., Moroi, K., Domingue, D., Michel, P., Pilorget, C., Iwata, T., Abe, M., Otake, M., Nakauchi, Y., Tsumura, K., Yabuta, H., Ishihara, Y., Noguchi, R., Matsumoto, K., Miura, A., Namiki, N., Tachibana, S., Arakawa, M., Ikeda, H., Wada, K., Mizuno, T., Hirose, C., Hosoda, S., Mori, O., Shimada, T., Soldini, S., Tsukizaki, R., Yano, H., Ozaki, M., Takeuchi, H., Yamamoto, Y., Okada, T., Shimaki, Y., Shirai, K., Iijima, Y., Noda, H., Kikuchi, S., Yamaguchi, T., Ogawa, N., Ono, G., Mimasu, Y., Yoshikawa, K., Takahashi, T., Takei, Y., Fujii, A., Nakazawa, S., Terui, F., Tanaka, S., Yoshikawa, M., Saiki, T., Watanabe, S., Tsuda, Y., 2020. Sample collection from asteroid (162173) Ryugu by Hayabusa2: implications for surface evolution. *Science* 368, 654–659.
- Moroz, L., Baratta, G., Strazzulla, G., Starukhina, L., Dotto, E., Barucci, M.A., Arnold, G., Distefano, E., 2004. Optical alteration of complex organics induced by ion irradiation: 1. Laboratory experiments suggest unusual space weathering trend. *Icarus* 170, 214–228.
- Moroz, L.V., Starukhina, L.V., Rout, S.S., Sasaki, S., Helbert, J., Baither, D., Bischoff, A., Hiesinger, H., 2014. Space weathering of silicate regoliths with various FeO contents: new insights from laser irradiation experiments and theoretical spectral simulations. *Icarus* 235, 187–206.
- Morris, R.V., 1976. Surface exposure indices of lunar soils: a comparative FMR study. In: Proceedings of the 7<sup>th</sup> Lunar Science Conference, pp. 315–335.
- Morris, R.V., Lauer, H.V., Lawson, C.A., Gibson, E.K., Nace, G.A., Stewart, C., 1985. Spectral and other physicochemical properties of submicron powders of hematite ( $\alpha$ -Fe2O3), maghemite ( $\gamma$ -Fe2O3), magnetite (Fe3O4), goethite ( $\alpha$ -FeOOH) and lepidocrocite ( $\gamma$ -FeOOH). *J. Geophys. Res.* 90, 3126–3144.
- Morris, R.V., Clark, J.V., Lee, S., Keller, L.P., Agresti, D.G., Archer, P.D., 2020. X-ray diffraction and reflectance spectroscopy of Murchison powders (CM2) after thermal analysis under reducing conditions to final temperatures between 300 and 1300°C. In: 51<sup>st</sup> Lunar and Planetary Science Conference (Abstract # 2850).
- Murae, T., Masuda, A., Takahashi, T., 1990. Spectroscopic studies of acid-resistant residues of carbonaceous chondrites. *Proc. NIPR Symp. Antarct. Meteorites* 3, 211–219.
- Nakamura, T., Noguchi, T., Tanaka, M., Zolensky, M.E., Kimura, M., Tsuchiyama, A., Nakato, A., Ogami, T., Ishida, H., Uesugi, M., Yada, T., Shirai, K., Fujimura, A., Okazaki, R., Sandford, S.A., Ishibashi, Y., Abe, M., Okada, T., Ueno, M., Mukai, T., Yoshikawa, M., Kawaguchi, J., 2011. Itokawa dust particles: a direct link between S-Type asteroids and ordinary chondrites. *Science* 333, 1113–1116.
- Nakamura, T., Lantz, C., Nakauchi, Y., Amano, K., Brunetto, R., Matsumoto, M., Kobayashi, S., Matsuoka, M., Noguchi, T., Matsumoto, T., Zolensky, M.E., 2020. Irradiation-energy dependence on the spectral changes of hydrous C-type asteroids based on 4keV and 20keV He exposure experiments of Murchison CM chondrite. In: 51<sup>st</sup> Lunar and Planetary Science Conference (Abstract # 1310).
- Nakauchi, Y., Abe, M., Otake, M., Matsumoto, T., Tsuchiyama, A., Kitazato, K., Yasuda, K., Suzuki, K., Nakata, Y., 2021. The formation of H<sub>2</sub>O and Si-OH by H<sub>2</sub><sup>+</sup> irradiation in major minerals of carbonaceous chondrites. *Icarus* 355, 114140.
- Nesbitt, H.W., Bancroft, G.M., Pratt, A.R., Scaini, M.J., 1998. Sulfur and iron surface states on fractured pyrite surfaces. *Am. Mineral.* 83, 1067–1076.
- Noble, S.K., Keller, L.P., Pieters, C.M., 2005. Evidence of space weathering in regolith breccias I: lunar regolith breccias. *Meteorit. Planet. Sci.* 40, 397–408.
- Noble, S.K., Pieters, C.M., Keller, L.P., 2007. An experimental approach to understanding the optical effects of space weathering. *Icarus* 192, 629–642.
- Noguchi, T., Nakamura, T., Kimura, M., Zolensky, M.E., Tanaka, M., Hashimoto, T., Konno, M., Nakato, A., Ogami, T., Fujimura, A., Abe, M., Yada, T., Mukai, T., Ueno, M., Okada, T., Shirai, K., Ishibashi, Y., Okazaki, R., 2011. Incipient space weathering observed on the surface of Itokawa dust particles. *Science* 333, 1121–1125.
- Noguchi, T., Bridges, J.C., Hicks, L.J., Gurman, S.J., Kimura, M., Hashimoto, T., Konno, M., Bradley, J.P., Okazaki, R., Uesugi, M., Yada, T., Karouji, Y., Abe, M., Okada, T., Mitsunari, T., Nakamura, T., Kagi, H., 2014a. Mineralogy of four Itokawa particles collected from the first touchdown site. *Earth Planets Sp.* 66, 124.
- Noguchi, T., Kimura, M., Hashimoto, T., Konno, M., Nakamura, T., Zolensky, M.E., Okazaki, R., Tanaka, M., Tsuchiyama, A., Nakato, A., Ogami, T., Ishida, H., Sagae, R., Tsujimoto, S., Matsumoto, T., Matsuno, J., Fujimura, A., Abe, M., Yada, T., Mukai, T., Ueno, M., Okada, T., Shirai, K., Ishibashi, Y., 2014b. Space weathered rims found on the surfaces of the Itokawa dust particles. *Meteorit. Planet. Sci.* 49, 188–214.
- Ondrusek, J., Christensen, P.R., Fink, J.H., 1993. Mapping the distribution of vesicular textures on silicic lavas using the Thermal Infrared Multispectral Scanner. *J. Geophys. Res.* 98.
- Pearson, V.K., Sephton, M.A., Franchi, I.A., Gibson, J.M., Gilmour, I., 2006. Carbon and nitrogen in carbonaceous chondrites: elemental abundances and stable isotopic compositions. *Meteorit. Planet. Sci.* 41, 1899–1918.
- Phakey, P.P., Hutcheon, I.D., Rajan, R.S., Price, P.B., 1972. Radiation effects in soils from five lunar missions. *Lunar Planet. Sci. Conf. Proc.* 3, 2905–2915.
- Pieters, C.M., Noble, S.K., 2016. Space weathering on airless bodies. *J. Geophys. Res. Planets* 121, 1865–1884.
- Pieters, C.M., Fischer, E.M., Rode, O., Basu, A., 1993. Optical effects of space weathering: the role of the finest fraction. *J. Geophys. Res.* 98, 20817–20824.
- Pieters, C.M., Taylor, L.A., Noble, S.K., Keller, L.P., Hapke, B., Morris, R.V., Allen, C.C., McKay, D.S., Wentworth, S., 2000. Space weathering on airless bodies: resolving a mystery with lunar samples. *Meteorit. Planet. Sci.* 35, 1101–1107.
- Pizzarello, S., Cooper, G.W., Flynn, G.J., 2006. The nature and distribution of the organic material in carbonaceous chondrites and interplanetary dust particles. In: Lauretta, D.S., McSween Jr., H.Y. (Eds.), *Meteorites and the Early Solar System II*. University of Arizona Press, Tucson, p. 943.
- Powell, C.J., Erickson, N.E., Madey, T.E., 1979. Results of a joint Auger-ESCA round robin sponsored by ASTM committee E-42 on surface analysis, I, ESCA results. *J. Electron Spectrosc. Relat. Phenom.* 361–403.
- Prince, B.S., Magnuson, M.P., Chaves, L.C., Thompson, M.S., Loeffler, M.J., 2020. Space weathering of FeS induced via pulsed laser irradiation. *J. Geophys. Res. Planets* 125, e2019JE006242.
- Ramsey, M.S., Fink, J.H., 1999. Estimating silicic lava vesicularity with thermal remote sensing: a new technique for volcanic mapping and monitoring. *Bull. Volcanol.* 61, 32–39.
- Rost, E., Hecker, C., Schodlok, M.C., van der Meer, F.D., 2018. Rock sample surface preparation influences thermal infrared spectra. *Minerals* 8, 1–21.
- Rouleau, F., Martin, P.G., 1991. Shape and clustering effects on the optical properties of amorphous carbon. *Astrophys. J.* 377, 526–540.
- Sakai, T., Nakamura, A., 2005. Quantification of porosity and surface roughness in laboratory measurements of the bidirectional reflectance of asteroid surface analogues. *Earth, Planets Sp.* 57, 71–76.
- Sasaki, S., Nakamura, K., Hamabe, Y., Kurahashi, E., Hiroi, T., 2001. Production of iron nanoparticles by laser irradiation in a simulation of lunar-like space weathering. *Nature* 410, 555–557.
- Schaible, M.J., Baragiola, R.A., 2014. Hydrogen implantation in silicates: the role of solar wind in SiOH bond formation on the surfaces of airless bodies in space. *J. Geophys. Res. Planets* 119, 2017–2028.

- Schmitt-Kopplin, P., Gabelica, Z., Gougeon, R.D., Fekete, A., Kanawati, B., Harir, M., Gebefuegi, I., Eckel, G., Hertkorn, N., 2010. High molecular diversity of extraterrestrial organic matter in Murchison meteorite revealed 40 years after its fall. *Proc. Natl. Acad. Sci. U. S. A.* 107, 2763–2768.
- Septon, M.A., 2002. Organic compounds in carbonaceous meteorites. *Nat. Prod. Rep.* 19, 292–311.
- Shi, Y.J., Lipson, R.H., 2005. An overview of organic molecule soft ionization using vacuum ultraviolet laser radiation. *Can. J. Chem.* 83, 1891–1902.
- Sigmund, P., 1979. Recoil implantation and ion-beam-induced composition changes in alloys and compounds. *J. Appl. Phys.* 50, 7261.
- Sigmund, P., 1981. Sputtering by ion bombardment: theoretical concepts. In: Behrisch, R. (Ed.), *Sputtering by Particle Bombardment I*. Springer-Verlag Berlin Heidelberg, pp. 9–71.
- Starukhina, L.V., Shkuratov, Y.G., Kodina, L.A., Ogleblina, A.I., Stankevich, N.P., Peregon, T.I., Tishchenko, L.P., 1990. Radiation-induced formation of polycyclic aromatic hydrocarbons (PAH's) on graphite surface: implication for cosmic dust and bodies. In: 21<sup>st</sup> Lunar and Planetary Science Conference, pp. 1192–1193.
- Takigawa, A., Asada, Y., Nakauchi, Y., Matsumoto, T., Tsuchiya, A., Abe, M., Watanabe, N., 2019. H<sup>+</sup> ion irradiation experiments of enstatite: space weathering by solar wind. In: 82<sup>nd</sup> Annual Meeting of The Meteoritical Society (Abstract # 6331).
- Takir, D., Emery, J.P., McSween, H.Y., Hibbitts, C.A., Clark, R.N., Pearson, N., Wang, A., 2013. Nature and degree of aqueous alteration in CM and CI carbonaceous chondrites. *Meteorit. Planet. Sci.* 48, 1618–1637.
- Terranova, U., Mitchell, C., Sankar, M., Morgan, D., de Leeuw, N.H., 2018. Initial oxygen incorporation in the prismatic surfaces of troilite FeS. *J. Phys. Chem. C* 122, 12810–12818.
- Thomas, J.E., Skinner, W.M., Smart, R.S.C., 2003. A comparison of the dissolution behavior of troilite with other iron(II) sulfides; implications of structure. *Geochim. Cosmochim. Acta* 67, 831–843.
- Thompson, M.S., Christoffersen, R., Zega, T.J., Keller, L.P., 2014. Microchemical and structural evidence for space weathering in soils from asteroid Itokawa. *Earth, Planets Sp.* 66, 89.
- Thompson, M.S., Zega, T.J., Howe, J.Y., 2017. In situ experimental formation and growth of Fe nanoparticles and vesicles in lunar soil. *Meteorit. Planet. Sci.* 52, 413–427.
- Thompson, M.S., Loeffler, M.J., Morris, R.V., Keller, L.P., Christoffersen, R., 2019. Spectral and chemical effects of simulated space weathering of the Murchison CM2 carbonaceous chondrite. *Icarus* 319, 499–511.
- Thompson, M.S., Morris, R.V., Clemett, S.J., Loeffler, M.J., Trang, D., Keller, L.P., Christoffersen, R., Agresti, D.G., 2020. The effect of progressive space weathering on the organic and inorganic components of a carbonaceous chondrite. *Icarus* 346, 113775.
- Vander Wal, R.L., Bryg, V.M., Hays, M.D., 2011. XPS analysis of combustion aerosols for chemical composition, surface chemistry, and carbon chemical state. *Anal. Chem.* 83, 1924–1930.
- Vernazza, P., Fulvio, D., Brunetto, R., Emery, J.P., Dukes, C.A., Cipriani, F., Witasse, O., Schäuble, M.J., Zanda, B., Strazzulla, G., Baragiola, R.A., 2013. Paucity of Tagish Lake-like parent bodies in the asteroid belt and among Jupiter Trojans. *Icarus* 225, 517–525.
- Wang, L.M., Ewing, R.C., 1992. Ion-beam-induced amorphization of complex ceramic materials—minerals. *MRS Bull.* 17, 38–44.
- Wang, L.M., Miller, M.L., Ewing, R.C., 1993. HRTEM study of displacement cascade damage in krypton-ion-irradiated silicate-olivine. *Ultramicroscopy* 51, 339–347.
- Watanabe, S., Tsuda, Y., Yoshikawa, M., Tanaka, S., Saiki, T., Nakazawa, S., 2017. Hayabusa2 mission overview. *Space Sci. Rev.* 208, 3–16.
- Wehner, G., 1959. Influence of the angle of incidence on sputtering yields. *J. Appl. Phys.* 30, 1762–1765.
- Yamada, M., Sasaki, S., Nagahara, H., Fujiwara, A., Hasegawa, S., Yano, H., Hiroi, T., Ohashi, H., Otake, H., 1999. Simulation of space weathering of planet-forming materials: nanosecond pulse laser irradiation and proton implantation on olivine and pyroxene samples. *Earth Planets Sp.* 51, 1255–1265.
- Yin, L., Tsang, T., Adler, I., 1976. On the ion-bombardment reduction mechanism. In: Proceedings of the 7<sup>th</sup> Lunar Science Conference, pp. 891–900.
- Ziegler, J.F., Ziegler, M.D., Biersack, J.P., 2010. SRIM - the stopping and range of ions in matter (2010). *Nucl. Inst. Methods Phys. Res. Sect. B Beam Interact. Mater. Atoms* 268, 1818–1823.
- Zolensky, M., McSween Jr., H.Y., 1988. Aqueous alteration. In: Kerridge, J.F., Matthews, M.S. (Eds.), *Meteorites and the Early Solar System*. University of Arizona Press, Tucson, pp. 114–143.
- Zolensky, M., Barrett, R., Browning, L., 1993. Mineralogy and composition of matrix and chondrule rims in carbonaceous chondrites. *Geochim. Cosmochim. Acta* 57, 3123–3148.